# Acoustic Propagation in the Near-Surface Martian Atmosphere

Martin Gillier, Andi Petculescu, Alexander E. Stott, Naomi Murdoch, Xavier Jacob, Baptiste Chide, Sylvestre Maurice, David Mimoun

▶ **To cite this version:**

Martin Gillier, Andi Petculescu, Alexander E. Stott, Naomi Murdoch, Xavier Jacob, et al.. Acoustic Propagation in the Near-Surface Martian Atmosphere. Journal of Geophysical Research: Planets, 2024, 129, 10.1029/2024JE008469 . insu-04833964

**HAL Id: insu-04833964**

**https://insu.hal.science/insu-04833964v1**

Submitted on 12 Dec 2024

**HAL** is a multi-disciplinary open access archive for the deposit and dissemination of scientific research documents, whether they are published or not. The documents may come from teaching and research institutions in France or abroad, or from public or private research centers.

L'archive ouverte pluridisciplinaire **HAL**, est destinée au dépôt et à la diffusion de documents scientifiques de niveau recherche, publiés ou non, émanant des établissements d'enseignement et de recherche français ou étrangers, des laboratoires publics ou privés.

Distributed under a Creative Commons Attribution - NonCommercial - NoDerivatives 4.0 International License

Check for updates

JGR Planets

RESEARCH ARTICLE

10.1029/2024JE008469

# Acoustic Propagation in the Near-Surface Martian Atmosphere

**Martin Gillier[1], Andi Petculescu[2], Alexander E. Stott[1], Naomi Murdoch[1], Xavier Jacob[3], Baptiste Chide[4], Sylvestre Maurice[4], and David Mimoun[1]**

[1]Institut Supérieur de l'Aéronautique et de l'Espace (ISAE-SUPAERO), Université de Toulouse, Toulouse, France, [2]Department of Physics, University of Louisiana at Lafayette, Lafayette, LA, USA, [3]Institut de Mécanique des Fluides de Toulouse, Université de Toulouse III Paul Sabatier, INP, CNRS, Toulouse, France, [4]Institut de Recherche en Astrophysique et Planétologie (IRAP), Université de Toulouse 3 Paul Sabatier, CNRS, CNES, Toulouse, France

**Key Points:**

- We have developed a model to compute the sound field created by a specific sound source at any time and place near the Martian surface
- Model predictions show that the main parameters affecting sound propagation are the temperature and wind speed profiles
- Refraction and atmospheric turbulence have a small effect on acoustic waves at the altitude of the Ingenuity rotorcraft

**Correspondence to:**

M. Gillier,
martin.gillier@isae-supaero.fr

**Citation:**

Gillier, M., Petculescu, A., Stott, A. E., Murdoch, N., Jacob, X., Chide, B., et al. (2024). Acoustic propagation in the near-surface Martian atmosphere. *Journal of Geophysical Research: Planets*, *129*, e2024JE008469. https://doi.org/10.1029/2024JE008469

Received 29 APR 2024
Accepted 2 JUL 2024

**Abstract** This work introduces a comprehensive model of sound propagation on Mars, in light of the recent operation of several microphones on the Martian surface. The main outcome of this work is an operational acoustic model capable of simulating the sound field created by any source, at any location on the Martian surface, at any time. Expanding on the result of previous work (Gillier et al., 2024, https://doi.org/10.1029/2023je008257), we use the parabolic equation method for sound propagation in order to obtain the overall sound field produced by a source, in a given atmospheric composition and state, and accounting for ground properties. The resulting model enables the study of acoustics on Mars, and has the potential also to be used to probe the properties of the Martian environment using acoustic measurements with known sources. We investigate the effects of the Martian ground and the vertical profile of temperature and wind, on sound propagation. We find that the ground has a minor effect on sound propagation, and the wind profile strongly influences sound propagation as on Earth. However, the midday near surface temperature profiles on Mars are shown to cause refraction, which generates non-negligible acoustic losses that are an order of magnitude stronger than typical refraction-related acoustic losses on Earth. We show that the effect of the Martian atmospheric turbulence is to slightly reduce the acoustic losses due to refraction. Finally, we apply our model to show that refraction and atmospheric turbulence have a negligible effect on the propagation of sound from Ingenuity to the Perseverance rover.

**Plain Language Summary** Sound provides new ways for exploring the Martian environment. Whether to examine the characteristics of sound sources on Mars or to infer atmospheric properties from the behavior of sound waves in the Martian atmosphere, an accurate model of sound propagation on Mars is needed. This model must account for the path traveled by the sound waves in the atmosphere as well as their interactions with the planet's surface. We propose a model that allows us to compute the sound that would be received by a microphone depending on its relative position to a source given a set of atmospheric conditions. We investigate the effects of the ground, the vertical gradient of temperature and the wind speed, as well as the effects of atmospheric turbulence. We find that, because of the strong temperature gradient at noon on Mars, sound is bent upwards creating a quieter zone close to the ground. This effect also occurs on Earth, but is much stronger on Mars. The main outcome of this work is a model that can simulate the sound field created by any source for any location at the Martian surface at any time of year and any time of day.

## 1. Introduction

Due to the inherent connection between sound and its transmission medium, acoustics has emerged as a reliable tool for investigating atmospheric characteristics. Drawing on decades of successful application in studying Earth's atmosphere, the scientific community has extended the use of acoustic techniques to explore the atmospheres of other planets. Previous research has underscored the value of acoustics in planetary exploration (Leighton & Petculescu, 2008), encompassing applications from sonar (Ainslie & Leighton, 2016) to probing the vertical structure of outer planet atmospheres (Lorenz, 1998). During the Soviet missions Venera 13 and 14, microphones recorded wind-induced noise on the surface of Venus (Ksanfomaliti et al., 1982). The Huygens probe that landed on Titan was equipped with various acoustic instruments, including a sonar (Towner et al., 2006) and a speed of sound sensor (Hagermann et al., 2007). Mars Polar Lander (1999, Albee et al., 2000) and Phoenix (2008, P. H. Smith, 2004) both carried microphones that were either lost along with the probes or not

© 2024. The Author(s).
This is an open access article under the terms of the Creative Commons Attribution-NonCommercial-NoDerivs License, which permits use and distribution in any medium, provided the original work is properly cited, the use is non-commercial and no modifications or adaptations are made.

21699100, 2024, 7, Downloaded from https://agupubs.onlinelibrary.wiley.com/doi/10.1029/2024JE008469 by Cochrane France, Wiley Online Library on [12/12/2024]. See the Terms and Conditions (https://onlinelibrary.wiley.com/terms-and-conditions) on Wiley Online Library for rules of use; OA articles are governed by the applicable Creative Commons License

turned on due to instrument safety concerns. More recently, Mars has seen the operation of the Entry, Descent, and Landing (EDL) and SuperCam microphones (Mimoun et al., 2023) on NASA's Perseverance rover, as well as a microphone on the Chinese National Space Administration's Zhurong rover (Zou et al., 2021). These microphones have already provided insights into the acoustic properties of the Martian atmosphere, either by capturing sounds from artificial sources like the Ingenuity helicopter (Lorenz et al., 2023) and the Laser Induced Breakdown Spectroscopy (LIBS) experiment (Chide et al., 2022, 2023) or by recording signals generated by the Martian environment, such as wind patterns (Stott et al., 2023) and a dust devil with the associated saltation (Murdoch et al., 2022).

In this context, there is a need for a model that describes how sound travels across the Martian surface. Specifically, understanding the effects of sound propagation enables the study of the acoustic properties of a sound source. Conversely, when the source is known, analyzing the received signal allows for the examination of the properties of the medium through which the acoustic wave travels. In both situations, the knowledge of the link between the atmosphere's properties and the way an acoustic wave travels in it is required. For example, the model would aid the characterization of spacecraft generated noises for engineering diagnostics. Additionally, a sound propagation model can aid in establishing the specifications of an instrument by taking into account the characteristics of the intended sound source it aims to record.

In Gillier et al. (2024) we proposed a model to compute the acoustic attenuation and sound speed in the near-surface Martian atmosphere at any time and place. However, a sound wave traveling near the surface is not only attenuated by the atmosphere but also reflected by the ground and possibly refracted along its path. In this work, we build upon the result of Gillier et al. (2024) to construct a model that can account for these effects. Williams (2001) already considered the reflection of the sound waves on the ground and the effect of atmospheric turbulence by estimating the ranges of the sound amplitude fluctuations caused by turbulence and the ground reflection coefficient, but did not fully simulate the resulting sound fields. Petculescu and Lueptow (2007) also considered the effect of the ground when a sound wave is propagating vertically in the first 5 km of the atmosphere, to simulate the descent of a probe, but did not look closely at the sound propagation near the surface.

We propose a model to quantify the sound pressure level (SPL) received by a detector for a given sound source at a given time and location on the Martian surface. The discussion is focused on the near-surface, that is, the first 20 m of the Martian atmosphere, as the goal is to understand the acoustic environment in which landers, rovers, drones and any future crewed missions would operate. The method we use, described in Section 2, consists first in taking outputs of the Martian Climate Database (MCD, see Forget et al., 1999; Millour et al., 2018) to get all the relevant properties of the Martian atmosphere at the place and time of interest (Section 2.2). A first-principles acoustic model is then used to determine the attenuation coefficient and the speed of sound for a dry atmosphere at each point of the propagation space from the MCD output (Gillier et al., 2024). A model of the Martian ground as a porous medium is proposed to estimate the ground impedance (Section 2.4). Finally, these parameters are fed into a model of atmospheric sound propagation based on the Parabolic Equation (PE) method (Section 2.6). With this model we are then able to investigate the effects of different processes occurring at the Martian surface on sound propagation (Section 3). This includes the effects of the profile of temperature (Section 3.2), the vertical gradient of wind speed (Section 3.3) and the atmospheric turbulence (Section 3.4). We then use the model to simulate some specific cases of application (Section 4) namely a flight of the Ingenuity rotorcraft (Section 4.2) and the case of a descending sound source (Section 4.3).

## 2. Method

### 2.1. Overview of the Model

Figure 1 shows the context for a sound source located close from the Martian surface. The various phenomenons that have an impact on sound propagation, namely the presence of a ground surface, a temperature and a wind profile and atmospheric turbulence, are highlighted. Figure 2 presents the architecture of the model that was developed for this study to account for the effect of all this phenomenon on sound propagation.

In the current model architecture, the temperature and pressure for a certain time and location are extracted from the MCD, but in situ measurements can also be used when available. Likewise, the turbulent parameters are computed using temperature and wind speed profiles from the MCD (see Section 2.5), but in situ measurements of

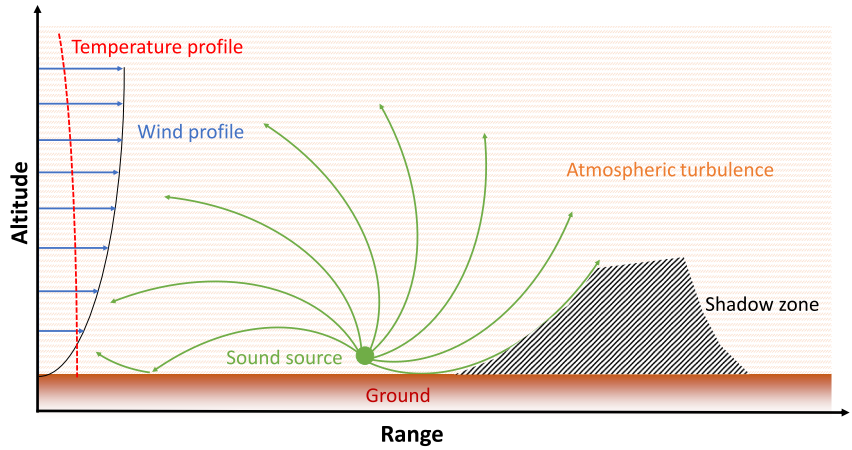


**Figure 1.** Context for a sound source located close from the Martian surface. The sound propagated from the source can be refracted by the wind and temperature profile, reflected by the ground and scattered by atmospheric turbulence. This can lead to the creation of a low sound level zone near the ground, the shadow zone. In this work, the altitude typically extends up to 20 m and the range up to 250 m.

these parameters can be used when available. One can vary each parameter of the general model individually to study its influence on the sound propagation. The results of this study are presented in Section 3.

### 2.2. Martian Atmospheric Parameterization: The Martian Climate Database

In this study, following classical definitions (Embleton, 1996), we define a homogeneous atmosphere as an environment in which the main ambient parameters (e.g., pressure, temperature, chemical composition, wind velocity) are the same throughout the simulation space. If the temperature or the wind velocity vary with altitude, we refer to it as a refractive atmosphere. A turbulent atmosphere is defined as an atmosphere in which the temperature, pressure and speed of sound exhibit short random fluctuations due to instability. If the magnitude of the turbulent fluctuations is the same everywhere, the turbulence is said to be homogeneous, whereas if it varies with altitude it is said to be inhomogeneous.

To infer steady-state values for all atmospheric parameters, we used the Martian Climate Database (MCD, see Forget et al., 1999; Millour et al., 2018). Pressure, temperature, wind velocity, chemical composition and other variables can be determined at a given latitude, longitude, altitude, time of year (expressed as a solar longitude, $L_s$) and time of day (expressed as Local True Solar Time, LTST) by interpolating between the stored data. The horizontal wind velocity and the temperature under the lowest layer (approximately 5 m above the surface) are computed using the Monin-Obukhov similarity theory (MOST).

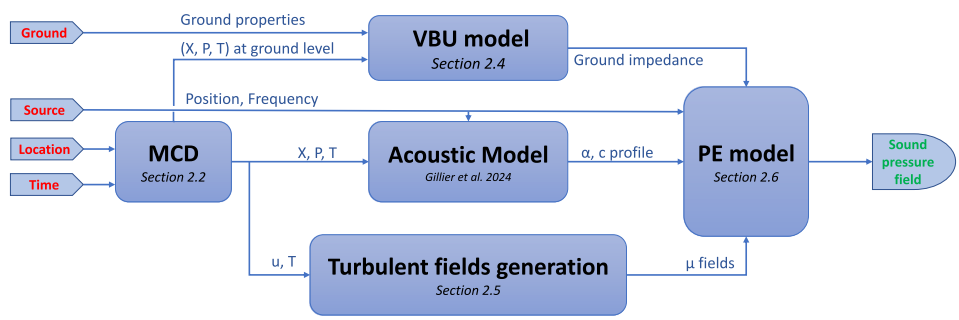


**Figure 2.** Architecture of the model used in this study. It shows how to use the MCD (Martian Climate Database) to retrieve the atmosphere chemical composition $X$, wind speed $u$, pressure $P$ and temperature $T$ and feed them into the model presented in Gillier et al. (2024) to compute sound speed $c$ and attenuation $\alpha$ in the atmosphere. The VBU (Venegas-Boutin-Umnova) model is used to predict porous regolith effects on acoustic waves, and the PE (Parabolic Equation) to obtain the overall sound field. The process of generating turbulent field of the refractive index $\mu$ is described in Section 2.5.



21699100, 2024, 7, Downloaded from https://agupubs.onlinelibrary.wiley.com/doi/10.1029/2024JE008469 by Cochrane France, Wiley Online Library on [12/12/2024]. See the Terms and Conditions (https://onlinelibrary.wiley.com/terms-and-conditions) on Wiley Online Library for rules of use; OA articles are governed by the applicable Creative Commons License

21699100, 2024, 7, Downloaded from https://agupubs.onlinelibrary.wiley.com/doi/10.1029/2024JE008469 by Cochrane France, Wiley Online Library on [12/12/2024]. See the Terms and Conditions (https://onlinelibrary.wiley.com/terms-and-conditions) on Wiley Online Library for rules of use; OA articles are governed by the applicable Creative Commons License

**Table 1**
*The Standard Martian Atmosphere Used in This Paper*

| Molecule | Molar fraction (%) |
|---|---|
| $CO_2$ | 96 |
| $N_2$ | 1.89 |
| Ar | 1.93 |
| $O_2$ | 0.145 |
| $H_2O$ | 0 |

*Note*. The values shown in this table were retrieved by the Curiosity rover (Mahaffy et al., 2013) and are used as the default chemical composition.

In this work, when a time and location are specified, atmospheric data from the MCD are used. If not, pressure and temperature are specified and the composition of the Martian atmosphere used is the standard one described in Table 1. Note that only dry atmospheres are considered, so in any case the molar fraction of $H_2O$ is equal to zero (see Gillier et al., 2024 for a discussion on this point).

### 2.3. Attenuation Coefficient and Speed of Sound

In a spherical harmonic wave of angular frequency $\omega$, the sound pressure fluctuations $p$ are described by

$$p(r,t) = \frac{A_0}{r}\exp(-\alpha r)\exp[i(k_0 r - \omega t)] \quad (1)$$

where $k_0 = \omega/c$ with $c$ the speed of sound, is the real part of the wavenumber, $\alpha$ is the attenuation coefficient and $r$ is the distance to the source. $A_0$ is a constant expressed either in terms of volume flux, or the pressure received at a reference distance. They exhibit geometrical spreading, modeled by the $\frac{1}{r}$ factor and intrinsic attenuation modeled by an exponential decay with a constant $\alpha$ in $m^{-1}$.

In Gillier et al. (2024), we presented a method to derive $\alpha$ and $c$ for a sound wave of a given frequency. As a reminder, the main findings of that study that are relevant to this work are:

1. The attenuation of sound waves is predominantly impacted by temperature and to a lesser degree to pressure.
2. The speed of sound is most sensitive to temperature and at a second order to the atmosphere's chemical composition.
3. Consequently, the large diurnal cycle (more than 50 K (Martinez et al., 2017, 2023)) of temperature at the Martian surface is the main source of variation in the value of the attenuation coefficient that can be as much as three times greater during the hottest hours than during the coldest ones.
4. The diurnal cycle of air temperature profile in the first 20 m of the Martian creates important differences between the almost homogeneous speed of sound profiles at night and the strongly refractive one during the day.

A useful measure for the relative energy carried by an acoustic wave is represented by the sound pressure level (SPL):

$$L_p = 10\log_{10}\left(\frac{\langle p^2\rangle}{p_{ref}^2}\right) \quad (2)$$

where $\langle p^2\rangle$ is the time-averaged squared pressure (e.g., over one period for a harmonic wave or over a characteristic timescale for non-periodic signals); for atmospheric propagation, $p_{ref} = 20$ μPa is the standard lower threshold of human hearing. This is, therefore, a quantity specific to Earth acoustics, corresponding to 1 pW/m$^2$ in terms of acoustic intensity. In the absence of an alternative factor, we will use it for Mars, keeping in mind its origin. On Mars, the reference value of the acoustic intensity would be of 70 pW/m$^2$ for this same reference pressure, which means that 10 to 100 more source power is needed to reach the same acoustic pressure amplitude on Mars. Since the outputs of the model presented in this work are SPL field interpreted in dB relatively to an arbitrary source amplitude, the reference value does not necessarily need to be adapted to Mars.

**Table 2**
*The Two Model of Ground That Are Used in This Study With Their Structural Parameters*

| Parameter | Fine-grained regolith | Coarse-grained regolith |
|---|---|---|
| $r_p$ | 0.4 mm | 1.5 mm |
| $\phi_p$ | 0.15 | 0.15 |
| $r_m$ | 0.1 μm | 0.1 μm |
| $\phi_m$ | 0.1 | 0.1 |
| $D_e$ | 0 | 0 |
| $H_e$ | 0 | 0 |

### 2.4. Acoustic Impedance of the Ground and the Air

An acoustic wave is characterized by the ratio of the instantaneous pressure to the instantaneous particle velocity, called specific or characteristic impedance, which depends on medium properties but also on position or frequency in the general case. For spherical waves, there exists a phase lag between

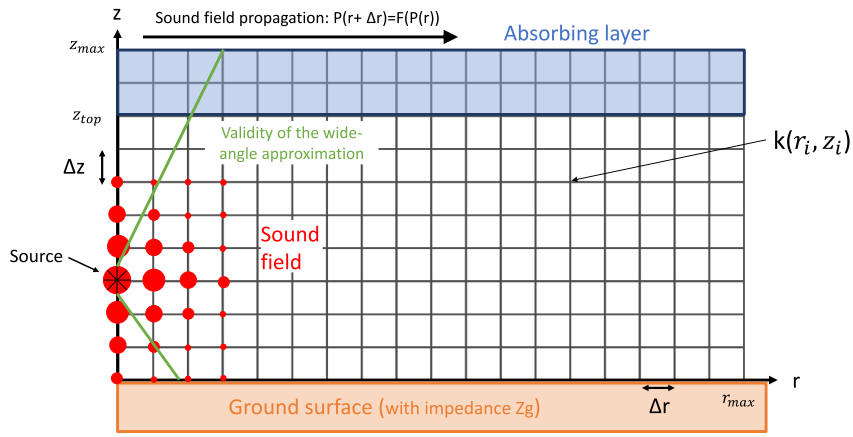


**Figure 3.** Grid in the (range, altitude) plane used in the parabolic equation method. The dots represent the sound field, the green lines represent the limit of the wide-angle approximation. $\Delta z$ is the grid step along the altitude ($z$) axis, $\Delta r$ is the grid step along the range ($r$) axis. Each point of the grid is associated with a complex wavenumber $k$.

pressure and velocity; as the wave propagates further away from the source, the two quantities become nearly in phase and the impedance approaches that of plane waves, $Z_{char} = \rho c$ where $\rho$ is the atmospheric density and c the speed of sound. When an acoustic wave encounters the interface between two different media, the reflected and transmitted fields depend on the characteristic impedance of each medium.

The acoustic signal detected by a microphone at height $z$ above the surface is generally the result of interference between the direct arrival and the reflected signal. The amplitude and phase of the reflected field depend on the flow behavior inside the porous ground, hence on (a) the gas thermophysical and transport properties and (b) the porous characteristics of the ground. This effect of the ground on the sound propagation is represented by its acoustic impedance.

At the surface of Mars, the atmospheric density is very small and thus the molecular mean free path can be as high as 50 µm (Hanford & Long, 2009). This means that the mean free path is of the same order of magnitude than the micropores present in the materials constituting the Martian ground, and thus that the absorption and desorption effects between the air circulating in the pores and the surface of the pores will be considerable. That is why we use the acoustic model for granular material presented in Venegas et al. (2017), which takes into account these effects. The Venegas-Boutin-Umnova (VBU) model has six inputs related to the material properties: the grain size $r_p$, the inter-granular porosity $\phi_p$, the micropore size $r_m$, the microporosity $\phi_m$ and two parameters related to the nanopores $D_e$ and $H_e$, the effective diffusion coefficient and linearized sorption equilibrium constant define in Venegas et al. (2017). The size of the particles that compose the regolith, defined here as unconsolidated deposit as opposed to bedrock, have been studied by different means. Study of the Phoenix optical microscope data (Goetz et al., 2010) has yield a distribution of particle size with two peaks, a fine one below 10 µm and a coarse one between 20 and 100 µm. Image analysis algorithm applied on Spirit rover regolith pictures have revealed a median grain size between 0.85 and 1.28 mm. Vaughan et al. (2023) studied close-up pictures of the Martian regolith at Jezero, where Perseverance is located. This demonstrated the existence of two kinds of regolith: fine-grained regolith with grain size between 80 and 530 µm and coarse-grained regolith with an average grain size between 1.01 and 1.88 mm. In the following, we will focus on a ground representative of what can be found at Perseverance site and use a fine-grained regolith with a grain size of 400 µm and a coarse-grained one with a grain size of 1.5 mm. It is difficult to estimate directly $\phi_p$ and $\phi_m$ for Martian regolith. However fitting humidity model to measurements at the surface of Mars allows the estimation of the total porosity $\phi$. This has given values of 0.16 at Phoenix site (Savijärvi et al., 2020), 0.3 at Curiosity site (Savijärvi et al., 2019) and 0.25 at Perseverance site (Polkko et al., 2023). Given that the relationship between the porosities is $\phi = \phi_p + (1 - \phi_p)\phi_m$ we have chosen to set $\phi_p$ to 0.15 and $\phi_m$ to 0.1 which give $\phi = 0.24$, a value in line with these references. Nanopores are not considered, thus $D_e = H_e = 0$. The ground properties used for the VBU model are summarized in Table 2.

The VBU model also requires several atmospheric parameters, namely the density $\rho$, viscosity $\eta$, thermal conductivity $\kappa$, heat capacity $C_p$ pressure $P$ and the speed of sound $c$ of the air flowing through the porous ground. All



21699100, 2024, 7, Downloaded from https://agupubs.onlinelibrary.wiley.com/doi/10.1029/2024JE008469 by Cochrane France, Wiley Online Library on [12/12/2024]. See the Terms and Conditions (https://onlinelibrary.wiley.com/terms-and-conditions) on Wiley Online Library for rules of use; OA articles are governed by the applicable Creative Commons License

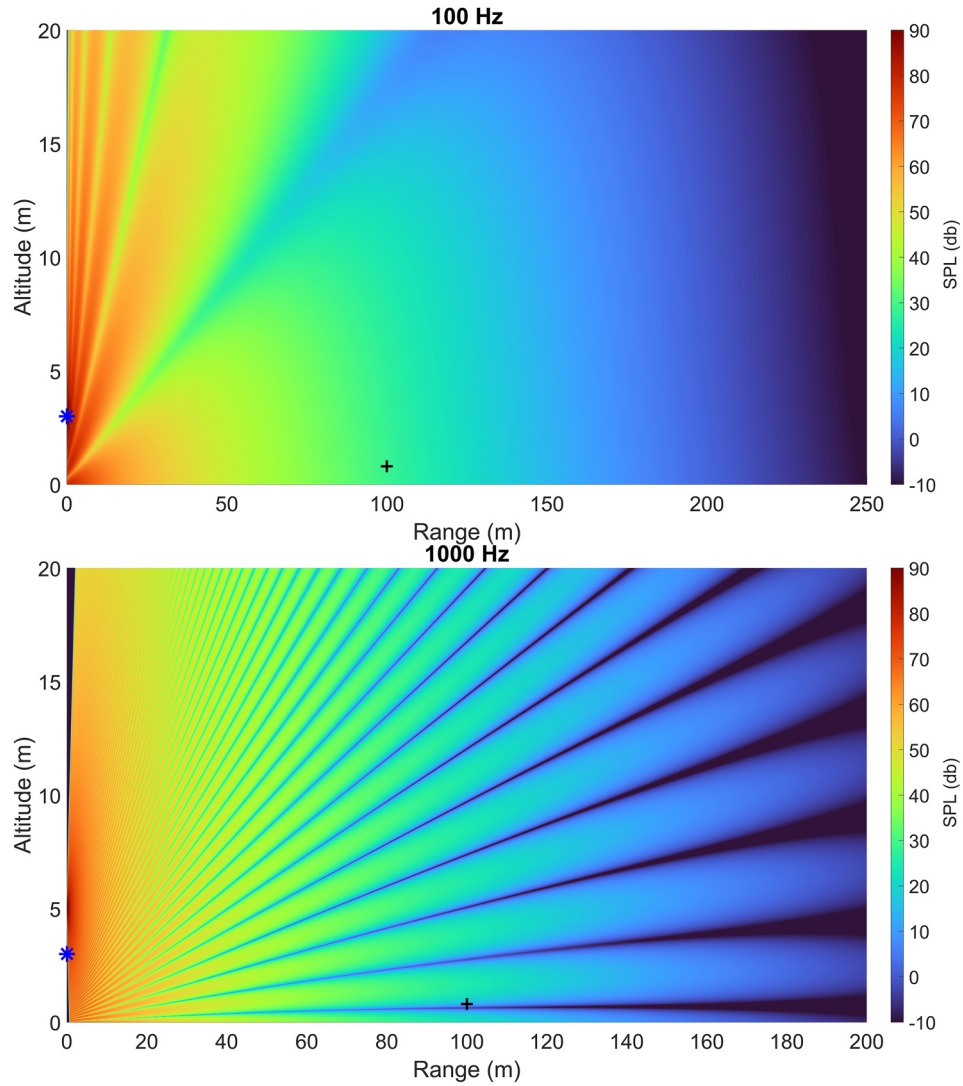


**Figure 4.** The result of two PE simulations, illustrating the effect of the ground on the propagation of a 100 Hz sound wave (top panel) and a 1,000 Hz one (bottom panel). The color scale shows the SPL at each point of the range-altitude plane in dB as defined in Equation 2. The source is 3 m above the ground (blue star). The atmospheric values were retrieved from the MCD at a solar longitude of 180° at 6 LTST at Perseverance site. The ground impedance was computed with the VBU model with the corresponding atmospheric parameters at the ground level and the coarse-grained regolith ground properties. The 1,000 Hz simulation was done with a 2 cm grid spacing.

of these parameters at ground level are extracted from the MCD or derived from the pressure temperature and chemical composition given by the MCD using data from Linstrom and Mallard (2023).

In summary, the VBU model allows for the computation of the ground impedance at a given frequency $Z_g(f)$ from the ground material structure and the atmospheric parameters at surface level. The normalized ground impedance $Z(f) = Z_g(f)/Z_{char}$ is used to take into account the effect of the ground on sound propagation (see Section 2.6).

In the following we will use only two classes of regolith to compute the ground impedance, the coarse grains and the fine grains as defined in Table 2. This is a simplification given that in reality, most of the Martian surface consists of a mixture of fine-grained and coarse-grained regolith with the fine-grained acting as a matrix for the coarser ones and that the Martian surface is far from being uniform with the presence of bedforms and bedrock slabs within the regolith (Vaughan et al., 2023).



21699100, 2024, 7, Downloaded from https://agupubs.onlinelibrary.wiley.com/doi/10.1029/2024JE008469 by Cochrane France, Wiley Online Library on [12/12/2024]. See the Terms and Conditions (https://onlinelibrary.wiley.com/terms-and-conditions) on Wiley Online Library for rules of use; OA articles are governed by the applicable Creative Commons License

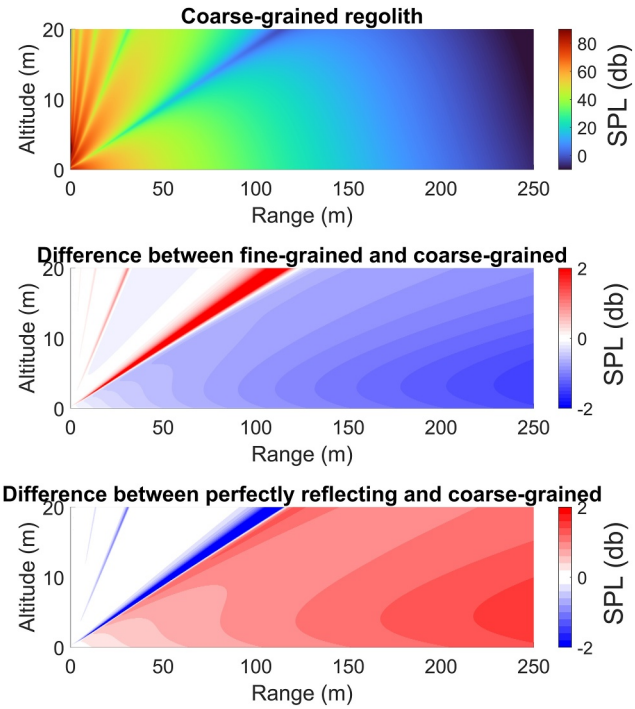


**Figure 5.** Comparison of the sound field produced by the same source, across the same atmosphere, over three different grounds. Top: the coarse-grained regolith, presented in Table 2. The color scale is the SPL at each point in dB, as in Figure 4. Middle: the difference between the top line simulation and the fine-grained regolith one. Bottom: the difference between the top line simulation and a perfectly reflecting ground. The colorbars for the middle and bottom lines correspond to a SPL difference in dB. The sound source is located at 3 m high with a level of 100 dB at 10 cm and the atmosphere was extracted from the MCD at Perseverance site at 6 LTST at a solar longitude of 180°.

**Table 3**
*Value of the Ground Normalized Impedance Z at 100 Hz for Different Air Temperature at the Ground Level ($T_g$) and Different Grain Size ($r_p$) for Coarse-Grained (CG) Regolith and Fined-Grained (FG) Regolith*

| $T_g$ (K) | $r_p$ CG (mm) | $r_p$ FG (μm) | $\phi_p$ | Z CG | Z FG |
|---|---|---|---|---|---|
| 200 | 1.5 | 400 | 0.15 | $118e^{0.4i}$ | $61e^{0.4i}$ |
| 240 | 1.5 | 400 | 0.15 | $108e^{0.4i}$ | $56e^{0.4i}$ |
| 300 | 1.5 | 400 | 0.15 | $100e^{0.4i}$ | $52e^{0.4i}$ |
| 240 | 1.01 | 80 | 0.15 | $89e^{0.4i}$ | $25e^{0.4i}$ |
| 240 | 1.5 | 400 | 0.15 | $108e^{0.3i}$ | $56e^{0.4i}$ |
| 240 | 1.88 | 530 | 0.15 | $121e^{0.4i}$ | $65e^{0.4i}$ |
| 240 | 1.5 | 400 | 0.1 | $163e^{0.1i}$ | $85e^{0.4i}$ |
| 240 | 1.5 | 400 | 0.3 | $54e^{0.1i}$ | $28e^{0.4i}$ |

*Note*. The phase of Z is related to the change in phase between the incident and the reflected sound.

### 2.5. Modeling Turbulence

A sound propagation method requires the knowledge of the field of the speed of sound. This field is not constant with time due to the fluctuation of certain atmospheric parameters, namely the temperature and the wind speed. If the timescale of the atmospheric parameter changes is long compared to the duration of the sound recording (typically a few minutes) this can be neglected. For example, the diurnal change of temperature occurs on a timescale of hours, thus it can be ignored for a recording of a length of a few minutes. However, the atmosphere can present quasi-random short-time fluctuations of the temperature and wind speed. This is known as atmospheric turbulence, and it has a strong impact on the propagation of sound.

Turbulent fluctuations are stochastic, and it is too difficult to resolve them explicitly. Thus, it is not relevant to look at an instantaneous sound field, as the sound fields change rapidly with the turbulent fluctuations. We can nevertheless estimate the effect of turbulence on the time-averaged sound fields. The time of averaging can typically be a few minutes long. The time-averaged sound pressure level can be approximated as the average of sound pressure levels produced by a certain number of sound waves going through a turbulent atmosphere. The atmosphere is different for each of the waves because of the turbulent fluctuations, but is constant during the propagation of one wave, because the sound wave's propagation time is small compared to the timescale of the turbulent fluctuations: this is the frozen medium approach.

Thus, one way to simulate the effect of atmospheric turbulence on the propagation of sound is to generate an ensemble of atmospheres according to the turbulence stochasticity around the steady-state atmosphere, propagate sound through them using the technique described in Section 2.6, and average the results (or, alternatively, look at their distribution if this is the result of interest). We have observed that the average sound field converges after 100 iterations, therefore this is the number of iterations that was used in the results presented here except if stated otherwise.

Instead of working with the speed of sound, it is usual to use the dimensionless refractive index $n$:

$$n = \frac{c_0}{c_{eff}} = \frac{c_0}{c + u\cos\theta} \tag{3}$$

with $c_0$ the speed of sound at the average temperature $T_0$, $c = c_0\sqrt{T/T_0}$ the adiabatic speed of sound and temperature T, and $u\cos\theta$ the wind speed in the propagation direction. Then in the case of a turbulent atmosphere:

$$n = \bar{n} + \mu \tag{4}$$

with $\bar{n}$ the average value of the refractive index over time and $\mu$ its fluctuation at a specific moment because of atmospheric turbulence. The issue is then to generate a series of $\mu$ fields that is representative of the actual Martian atmosphere.

A way to do so is to ensure that each field has the same spectral density as the actual field in the Martian atmosphere. A common way to represent atmospheric turbulence is the von Kármán spectrum that we used in this study. It must be noted, however, that what follows works with any turbulence



21699100, 2024, 7, Downloaded from https://agupubs.onlinelibrary.wiley.com/doi/10.1029/2024JE008469 by Cochrane France, Wiley Online Library on [12/12/2024]. See the Terms and Conditions (https://onlinelibrary.wiley.com/terms-and-conditions) on Wiley Online Library for rules of use; OA articles are governed by the applicable Creative Commons License

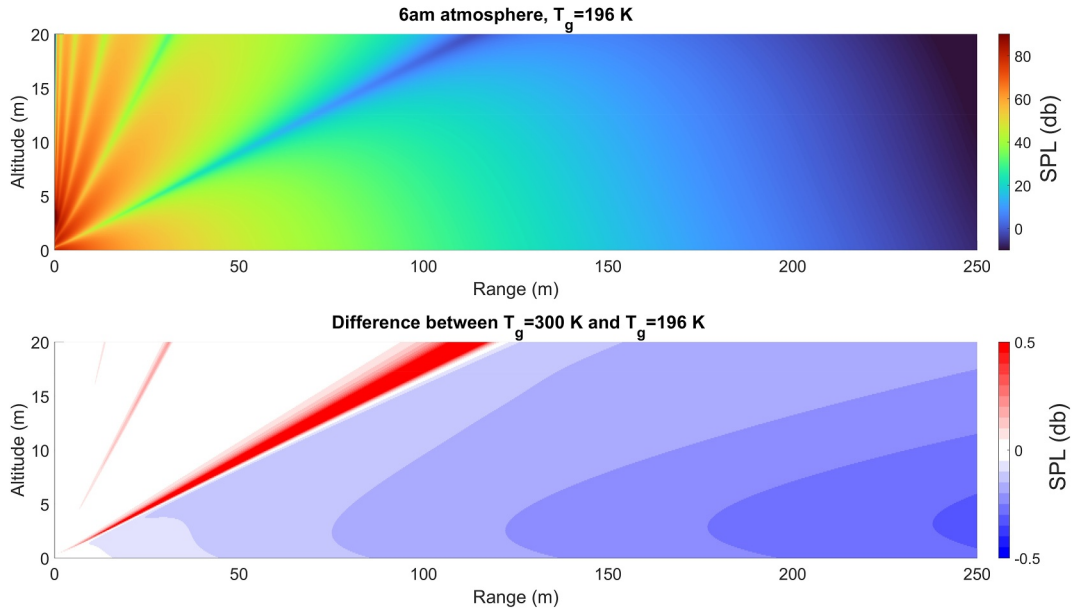


**Figure 6.** Comparison of the sound field produced by the same source, across the same atmosphere, over two different grounds. Top: a ground where the ground temperature $T_g$ is equal to 196 K. The color scale is the SPL at each point in dB, as in Figure 4. Bottom: difference between the top line simulation and one with a ground at $T_g$ = 300 K The color scale for bottom line corresponds to a SPL difference in dB. The sound source is located at 3 m high with a level of 100 dB at 10 cm and the atmosphere was extracted from the MCD at Perseverance site at 6 LTST at a solar longitude of 180°. The ground is the coarse-grained regolith presented in Table 2.

spectrum (e.g., Gaussian or Kolmogorov), and in an inverse problem approach it can be useful to vary the spectrum used to estimate which one is closest to measured results.

For isotropic turbulence, the von Kármán expression of the two-dimensional spectral density of the refractive-index fluctuation is (Salomons, 2001):

$$F(k) = \frac{1}{\left(k^2 + K_0^2\right)^{8/6}} \left( B_1 \frac{C_T^2}{T_0^2} + \left[ B_2 + B_3 \frac{k^2}{k^2 + K_0^2} \right] \frac{C_v^2}{c_0^2} \right) \tag{5}$$

with $B_1$, $B_2$, and $B_3$ numerical constants, characteristic of the type of spectrum that we assumed, whose value is given in Appendix A, $k$ the wave number, $K_0 = 2\pi/L$ with L the size of the largest eddies and $C_T^2$, $C_v^2$ the structure function parameters of the temperature and the wind speed:

$$C_T^2 = \frac{3\Gamma(5/6)}{\pi^{1/2}} \frac{\sigma_T^2}{L_T^{2/3}} \tag{6}$$

$$C_v^2 = \frac{3\Gamma(5/6)}{\pi^{1/2}} \frac{\sigma_v^2}{L_v^{2/3}} \tag{7}$$

The structure function parameters are characteristic of the atmospheric state and are thus strongly dependent on the planet, location and time of day. Computing the von Kármán spectrum, therefore, requires an estimation of the standard deviation of the fluctuation of temperature and wind speed and their length scales (respectively $\sigma_T$, $\sigma_v$, $L_T$, and $L_v$). There is no direct way to estimate these parameters from the outputs of the MCD. Moreover, it is difficult to measure the length scale at the surface of Mars, even if an acoustic experiment has allowed to investigate them (Chide et al., 2024). V. E. Ostashev (2016) presents a method to derive these parameters from similarity relations based on the MOST parameters. The detail of this method, as well as the way to obtain the MOST parameters from the outputs of the MCD, is described in Appendix B. Equations B2–B7 show that the turbulent parameters depend on the altitude and thus the turbulent spectrum F is a function of $k$ and $z$.



21699100, 2024, 7, Downloaded from https://agupubs.onlinelibrary.wiley.com/doi/10.1029/2024JE008469 by Cochrane France, Wiley Online Library on [12/12/2024]. See the Terms and Conditions (https://onlinelibrary.wiley.com/terms-and-conditions) on Wiley Online Library for rules of use; OA articles are governed by the applicable Creative Commons License

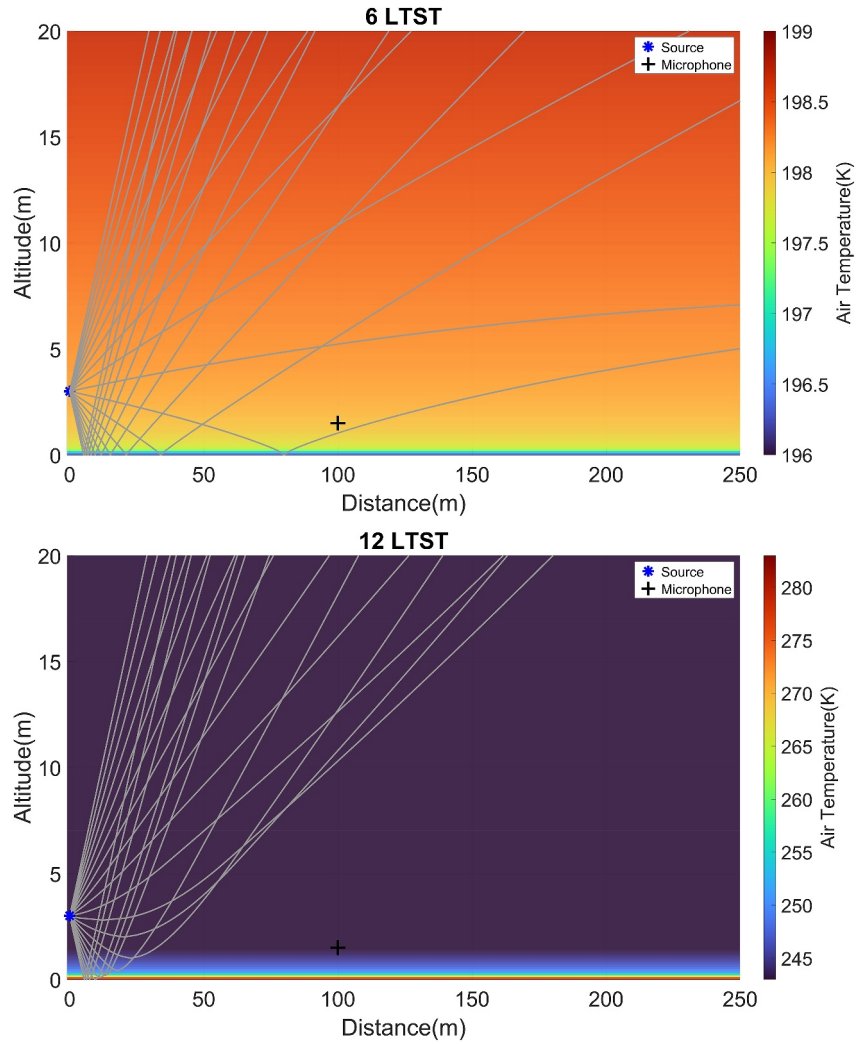


**Figure 7.** A ray model of the propagation of sound on the surface of Mars at 6 (a) and 12 (b) LTST. Gray lines are the rays propagated from the source. The colorbar correspond to the air temperature used in the simulation. The air temperature values were retrieved from the MCD at the Perseverance site at a solar longitude of 180°. The sound source is at 3 m from the ground.

From the spectrum, a $\mu$ field can be computed using the random-phase method (RPM). The idea of the RPM is to apply an inverse Fourier transform on the spectrum after having added a random phase at each mode. The $\mu$ field is then given by (see Salomons, 2001 appendix J):

$$\mu(r,z) = \sum_n \sqrt{4\pi\Delta k F(k_n)\, k_n} \cos\left(r k_n cos(\theta_n) + z k_n sin(\theta_n) + \alpha_n\right) \quad (8)$$

where $\theta_n$ and $\alpha_n$ are random angles. If F depends on the altitude, one can simply replace F(k) by F(k, z) following Dallois et al. (2001).

In summary, we model turbulence by propagating a sound wave across a variety of randomly fluctuating atmospheres. To do so, it is required to know certain parameters of the turbulent fluctuations of the wind speed $u$ and the temperature $T$. These parameters can be computed from similarity relations using temperature and wind velocity profile from the MCD. It must be noted that given the uncertainties on the determination of the turbulent parameters and the limitation of the random-phase method, the results obtained with the method presented in this section are merely an illustration of the effects of turbulence on sound propagation and should be treated with caution.



21699100, 2024, 7, Downloaded from https://agupubs.onlinelibrary.wiley.com/doi/10.1029/2024JE008469 by Cochrane France, Wiley Online Library on [12/12/2024]. See the Terms and Conditions (https://onlinelibrary.wiley.com/terms-and-conditions) on Wiley Online Library for rules of use; OA articles are governed by the applicable Creative Commons License

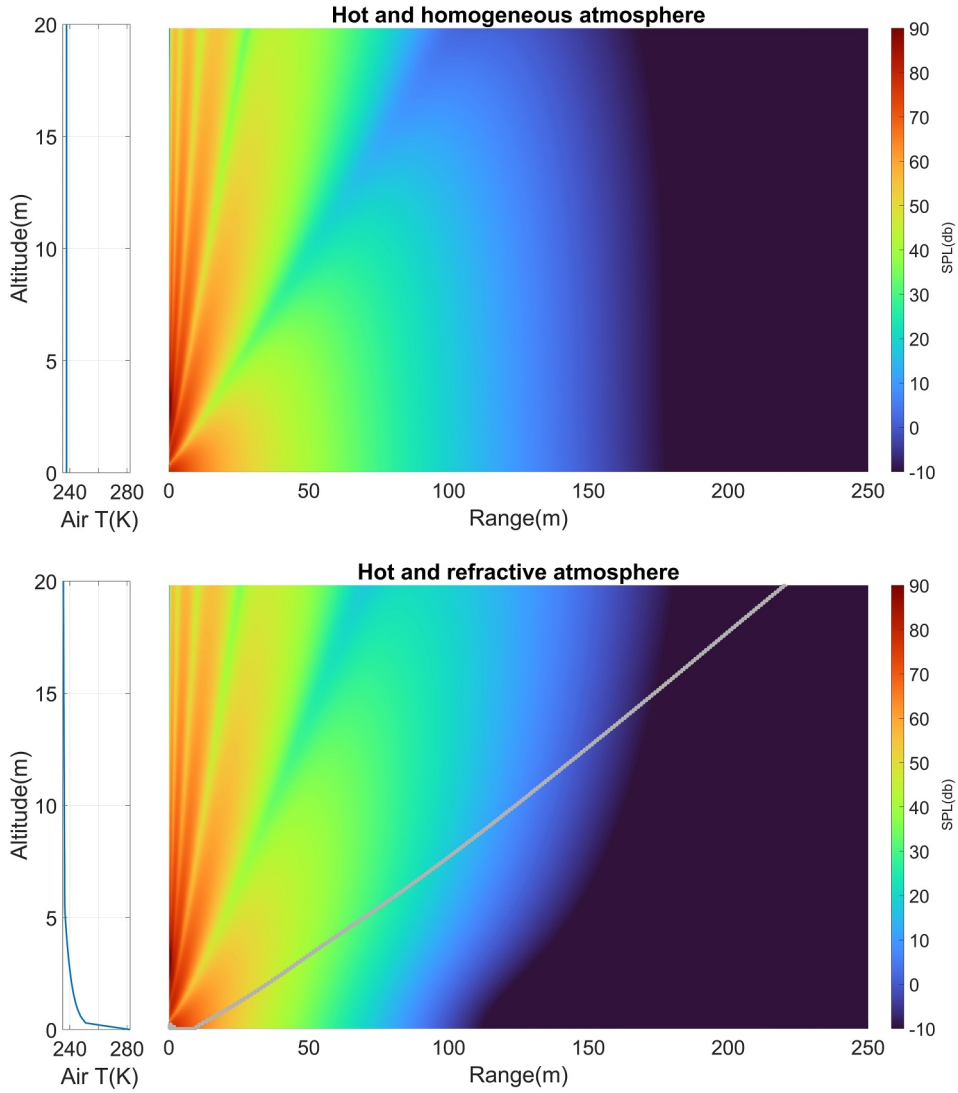


**Figure 8.** Simulated sound field on the surface of Mars for (top): a hot and homogeneous atmosphere and (bottom): a hot and refractive atmosphere (12 LTST). The color scale shows the SPL at each point of the range-altitude plane in dB as defined in Equation 2. The profile of air temperature used in the simulation are displayed on the left. All the atmospheric values were retrieved from the MCD at a solar longitude of 180°. The sound source has a frequency of 100 Hz, a level of 100 dB at 10 cm and is at 3 m from the ground. The gray line is the upper boundary of the shadow zone (see main text for definition).

### 2.6. The Parabolic Equation (PE) Method

The method used in this work to model the propagation of sound near the Martian surface is the Parabolic Equation (PE) method. The PE method is a proven and widely used numerical method to compute the sound field of a monochromatic spherical source over a ground surface (Gilbert & White, 1989). The sound is propagated in a 2D (range, altitude) plane as the method is based on the axisymmetric approximation, that is, all variables are considered constant with azimuth. The simulation space is thus the grid shown in Figure 3 with $r$ and $z$ the cylindrical coordinates. The idea is to start with the sound field created by the source at $r = 0$, and then to propagate it along the $r$ axis. Since results will be discussed in terms of transmission loss or excess attenuation, the amplitude of the source can be fixed arbitrarily. In the following, the source level is of 100 dB at 10 cm from the point source, which can be understood as the approximate order of magnitude of a UAV rotor noise on Mars (Lorenz et al., 2023).



21699100, 2024, 7, Downloaded from https://agupubs.onlinelibrary.wiley.com/doi/10.1029/2024JE008469 by Cochrane France, Wiley Online Library on [12/12/2024]. See the Terms and Conditions (https://onlinelibrary.wiley.com/terms-and-conditions) on Wiley Online Library for rules of use; OA articles are governed by the applicable Creative Commons License

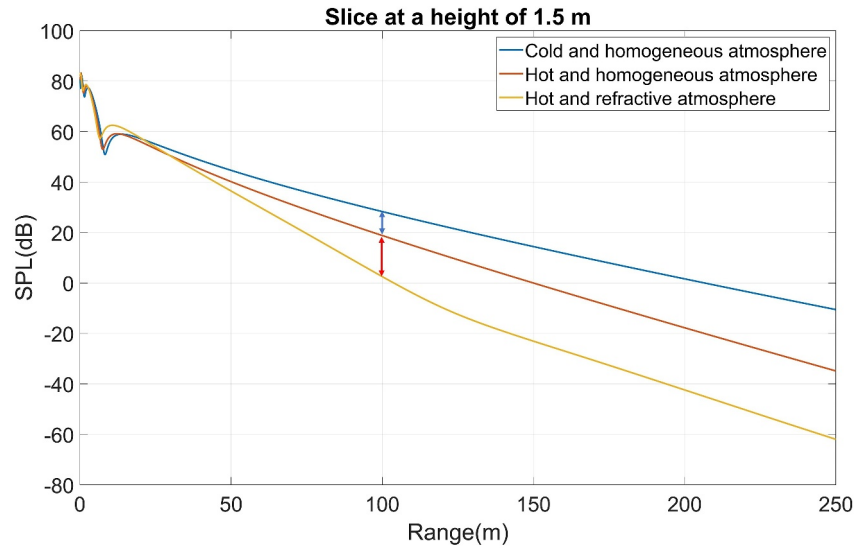


**Figure 9.** The sound pressure level extracted from the PE simulation presented in Figure 8 at a height of 1.5 m as a function of the horizontal distance from the source (horizontal slices of PE simulations). A cold and homogeneous atmosphere, which corresponds to the simulation at 6 LTST at Perseverance site has also been added for comparison with the effect of the diurnal cycle of temperature.

The sound equation in the far field ($r \gg {}_0^{-1}$, $k_0^{-1}$ around 40 cm for a 100 Hz wave near the Martian surface) becomes the two-dimensional Helmholtz differential equation when the axisymmetric assumption is applied

$$\frac{\partial^2 q}{\partial r^2} + \frac{\partial^2 q}{\partial z^2} + k_{eff}^2 q = 0 \tag{9}$$

where $q$ is related to the complex amplitude $q = p\sqrt{r}$ and $k_{eff} = \omega/c_{eff}$. The general solution is given as

$$q(r,z) = \psi(r,z)\exp(ik_a r)$$

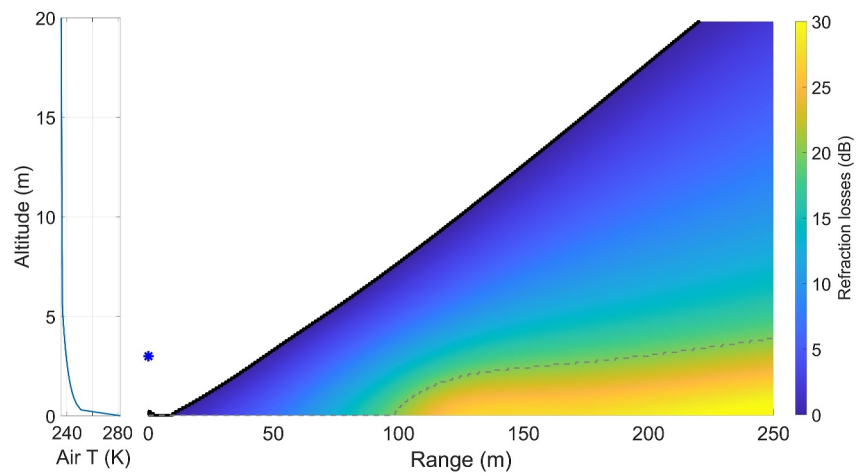


**Figure 10.** The depth of the shadow zone, that is, the difference of sound pressure level between the hot and homogeneous atmosphere and the hot and refractive atmosphere at each point of the range-altitude plane. The color scale corresponds to the additional losses in the SPL field induced by sound refraction in dB. The black line is the upper boundary of the shadow zone. Above the shadow zone, the SPL difference is generally negative to null, but it depends on the positions of the interference patterns. The dashed line defines the zone where the losses are greater than 20 dB. The blue star is the sound source. The temperature profile that caused the shadow zone is shown on the left.



21699100, 2024, 7, Downloaded from https://agupubs.onlinelibrary.wiley.com/doi/10.1029/2024JE008469 by Cochrane France, Wiley Online Library on [12/12/2024]. See the Terms and Conditions (https://onlinelibrary.wiley.com/terms-and-conditions) on Wiley Online Library for rules of use; OA articles are governed by the applicable Creative Commons License

21699100, 2024, 7, Downloaded from https://agupubs.onlinelibrary.wiley.com/doi/10.1029/2024JE008469 by Cochrane France, Wiley Online Library on [12/12/2024]. See the Terms and Conditions (https://onlinelibrary.wiley.com/terms-and-conditions) on Wiley Online Library for rules of use; OA articles are governed by the applicable Creative Commons License

where $k_a$ is the wavenumber at a given height. To numerically solve the sound field we write Equation 9 to a parabolic equation employing the wide angle approximations (see Salomons, 2001; West et al., 1992 section G for technical details). This parabolic equation can be solved using the Crank-Nicolson method, by approximating the derivative in $z$ by its finite difference and integrating over $r$. It gives the relationship that is needed to propagate the sound field along the r axis. For accurate results, the grid spacing $\Delta r$ and $\Delta z$ needs to be smaller than $\lambda/10$. Given that the average speed of sound at the Martian surface is around 240 m/s this means that the grid spacing needs to be smaller than 0.24 m for a 100 Hz sound. In all the simulations presented here, we used a 0.1 m spacing except if stated otherwise. This method is valid for an elevation angle smaller than 35°, which is represented by the green line in Figure 3.

The main input of the PE method is a grid of complex wavenumbers $k = k_0 + i\alpha$, and thus, a grid of attenuation coefficients and sound speeds. The fact that the speed of sound can be dependent on $z$ and $r$ can be used to simulate both refractive and turbulent atmospheres. The speed of sound can be written as $c_{eff} = c + u\cos(\theta)$ where $c$ is the thermal speed of sound (an output of the acoustic model, see Gillier et al., 2024), $u$ is the wind speed and $\theta$ is the angle between the direction of the wind and the direction in which the sound travels. Another input of the PE is the normalized ground impedance, the derivation of which is described in Section 2.4. An absorption layer with an artificially high attenuation coefficient is added on the top of the simulation. Thus, the simulation is valid between $z = 0$ and $z_{top}$, the altitude of the absorption layer. It is also possible to simulate sound propagation without the ground by replacing the ground layer by another absorption layer. The sound source is modeled by an initial Gaussian sound field (Salomons, 2001) at $r = 0$ and centered at the desired altitude. The PE method includes the geometrical attenuation of a spherical wave described in Equation 1.

In summary, we use the PE method to compute the sound field created by a monochromatic source given a specific surface (a ground impedance) and a specific atmosphere (a field of attenuation coefficient and speed of sound). This approach is valid in the far field ($r \gg k^{-1}$) for an elevation angle between −35° and +35° in the case where all acoustic waves are traveling from the source to the detector (no back-scattering or reflection from a vertical surface).

## 3. Results

The effect of parameters that affect the attenuation coefficient can be found in Gillier et al. (2024). In this paper, we investigate the effect of parameters that do not directly affect the attenuation coefficient but have an impact on the way sound propagate and thus on the resulting sound field. The effect of the ground (Section 3.1) is investigated first. We then go through the effects of the temperature profile (Section 3.2), the wind velocity profile (Section 3.3) and the atmospheric turbulence (Section 3.4). To do so, the sound coming from a 100 dB sound source located at 3 m above the ground is propagated through various Martian atmospheres.

Sound fields are shown between the ground at $z = 0$ to an altitude of $z = 20$ m, as this is where most of the relevant sound detectors (embedded on landers, rovers, and drones) would be located. The maximum range from the source has been set to 250 m, as it is unlikely that a sound would propagate further because of the very strong acoustic attenuation at the Martian surface (Bass & Chambers, 2001; Gillier et al., 2024; Petculescu & Lueptow, 2007; Williams, 2001). We have chosen to set the frequency to 100 Hz, unless specified otherwise, as this is representative of the sound produced by Ingenuity, the helicopter traveling along Perseverance rover (Lorenz et al., 2023). We have also chosen to show results at Perseverance site at a solar longitude of 180° as it will allow easier comparison with Perseverance data and the effects that are shown are weakly dependent on the location and the time of year.

The following results are not exhaustive, as this model can be used to study sound propagation in a wide variety of context, but they explore the main parameters that impact the sound field. A synthesis showing the relative importance of every parameter that was studied is presented in Section 3.5.

### 3.1. The Effect of the Martian Surface

Figure 4 shows outputs of the model. It represents the sound field created by a source at 3 m above the ground, represented by a blue star. This means that a microphone located at 0.8 m above the ground and 100 m away from the source (represented by the black cross) will sense an SPL of 30 dB for a 100 Hz wave and 10 dB for a 1 kHz wave.

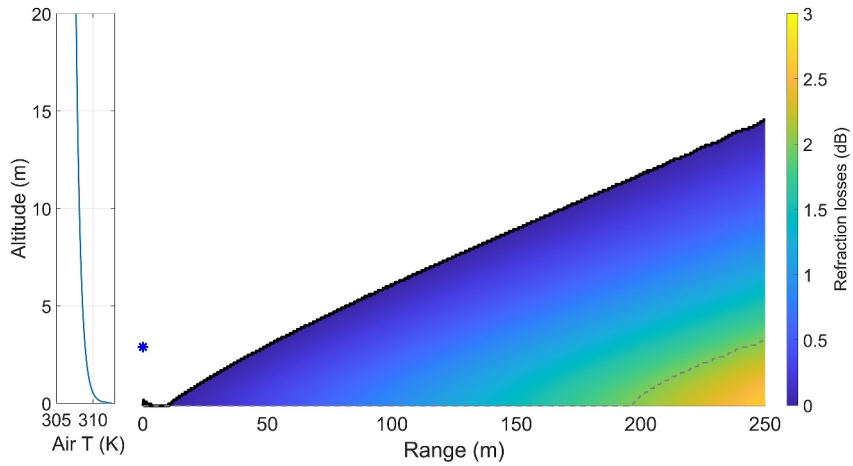


**Figure 11.** The depth of the shadow zone (see caption of Figure 10) at the Earth surface based on a temperature profile measured in Egypt in July at 1 p.m. (Flower, 1937; Geiger et al., 1995). The black line is the upper boundary of the shadow zone. The dashed line defines the zone where the losses are greater than 2 dB. The blue star is the sound source. The temperature profile that caused the shadow zone is shown on the left.

At each point of the range-altitude plane, the SPL is the result of the combination of a direct arrival and a reflected signal. The reflected signal is shifted in phase and thus at certain points the two signals will cancel, creating "interference patterns." It follows that the location and the number of these minima will depend on the wavelength of the acoustic wave.

Figure 4 shows these minima for a 100 Hz and a 1,000 Hz sound source. The shift in phase also depends on the ground impedance which in turn depends on the frequency (see Section 2.4). As explained in Section 2.4, the ground impedance varies with atmospheric parameters, notably the temperature and the pressure. However, these variations of the ground impedance with the atmospheric parameters are small compared to variations caused by the uncertainties on the ground properties, especially the grain size.

Table 3 presents a comparison of the changes in normalized impedance Z caused by an increase of temperature from 200 to 300 K and caused by an increase in grain size from 0.08 m to 0.530 mm (respectively 1.01–1.88 mm) for fine-grained regolith (respectively coarse-grained) that correspond to the uncertainties on the grain size (Vaughan et al., 2023). It also shows the changes caused by an increase of $\phi_p$ from 0.1 to 0.3 It shows that the change in $Z$ from this extreme variation of temperature is smaller than the change with grain size or with porosity.

To illustrate the impact of these changes in the normalized ground impedance on the sound field, the following Figures 5 and 6 show some PE simulations with a 100 Hz source where the ground and atmospheric parameters used to compute the ground impedance were changed. The atmosphere, however, is the same in each set of simulations.

First, Figure 5 shows the sound field over a coarse-grained regolith and the difference between the sound field over a fine-grained regolith and a coarse-grained regolith. The comparison with the case of an ideal perfectly reflecting ground with an infinite acoustic impedance is also shown for reference.

Figure 5 shows that the main effect of the changes in ground impedance is to slightly shift the position of the interference patterns and to modify their depth. The interference patterns are less marked in the fine-grained regolith grain and more marked in the perfectly reflecting case. Regarding the SPL field far away from the source, it is decreasing when the coarse-grained regolith is replaced by a fine-grained one and increasing when it is replaced by a perfectly reflecting ground. These variations are close to a factor of 1.5 on pressure amplitude (~3 dB), and the spatial distribution is also significantly changed.

Another parameter that impacts the ground impedance is the surface temperature, as shown in Table 3. To illustrate the impact of temperature driven ground impedance changes on the SPL field we have plotted in Figure 6 the sound field over a coarse-grained regolith with a ground temperature of 196 K and the difference between it and one propagated over a ground at 300 K. The effect of the change of ground impedance induced by



21699100, 2024, 7, Downloaded from https://agupubs.onlinelibrary.wiley.com/doi/10.1029/2024JE008469 by Cochrane France, Wiley Online Library on [12/12/2024]. See the Terms and Conditions (https://onlinelibrary.wiley.com/terms-and-conditions) on Wiley Online Library for rules of use; OA articles are governed by the applicable Creative Commons License

10.1029/2024JE008469

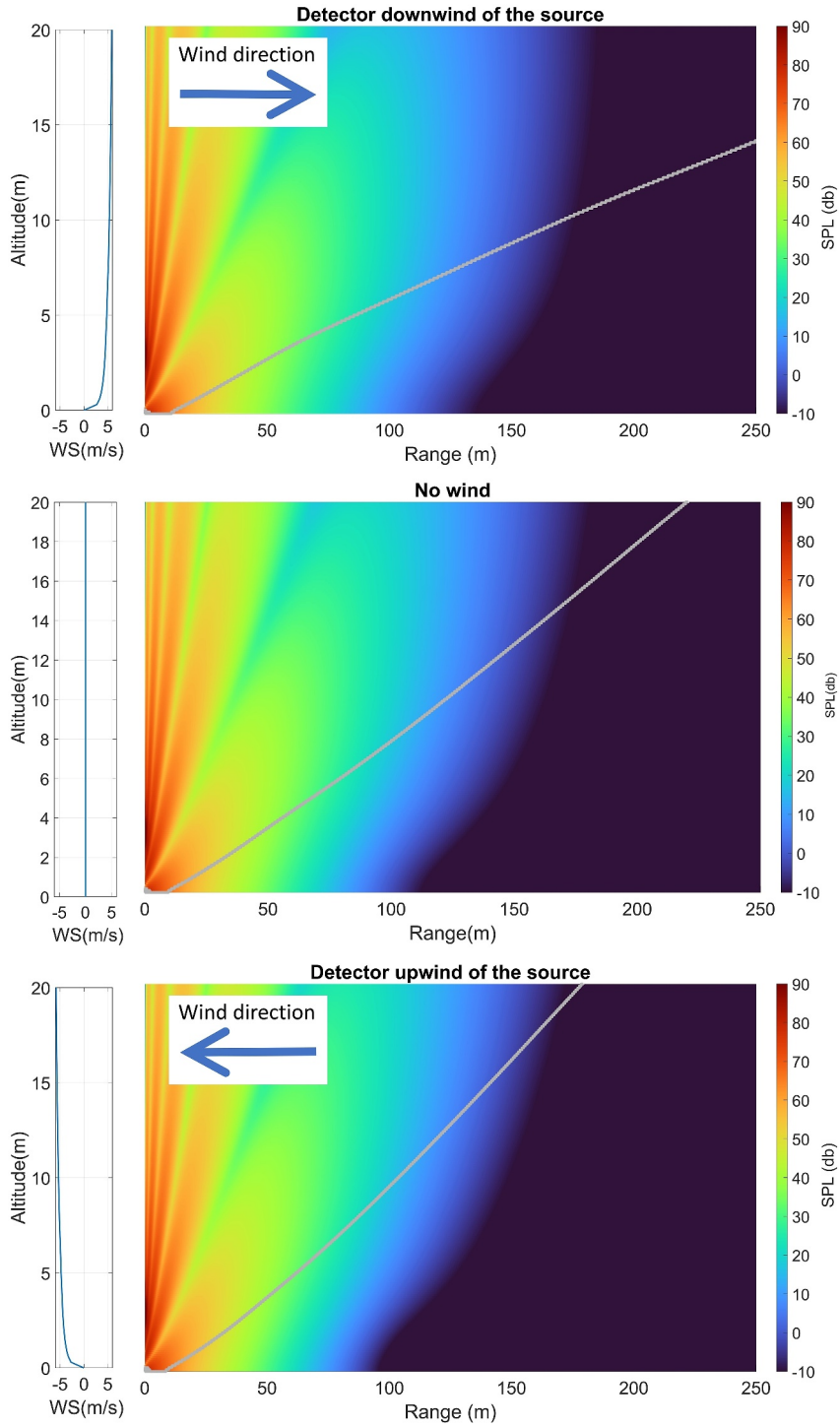


**Figure 12.** Simulated sound field on the surface of Mars at 12 LTST at a solar longitude of 180°. The color scale shows the SPL at each point of the range-altitude plane in dB as defined in Equation 2. The wind speed profile used in each simulation is displayed on the left. The wind speed is positive if the detector is downwind of the source. The gray lines correspond to the upper boundaries of the shadow zone. All the atmospheric values were retrieved from the MCD with the wind speed values scaled so to have a wind speed of 4 m/s at 1.5 m above the ground. The sound source has a frequency of 100 Hz, a level of 100 dB at 10 cm and is at 3 m from the ground.



21699100, 2024, 7, Downloaded from https://agupubs.onlinelibrary.wiley.com/doi/10.1029/2024JE008469 by Cochrane France, Wiley Online Library on [12/12/2024]. See the Terms and Conditions (https://onlinelibrary.wiley.com/terms-and-conditions) on Wiley Online Library for rules of use; OA articles are governed by the applicable Creative Commons License

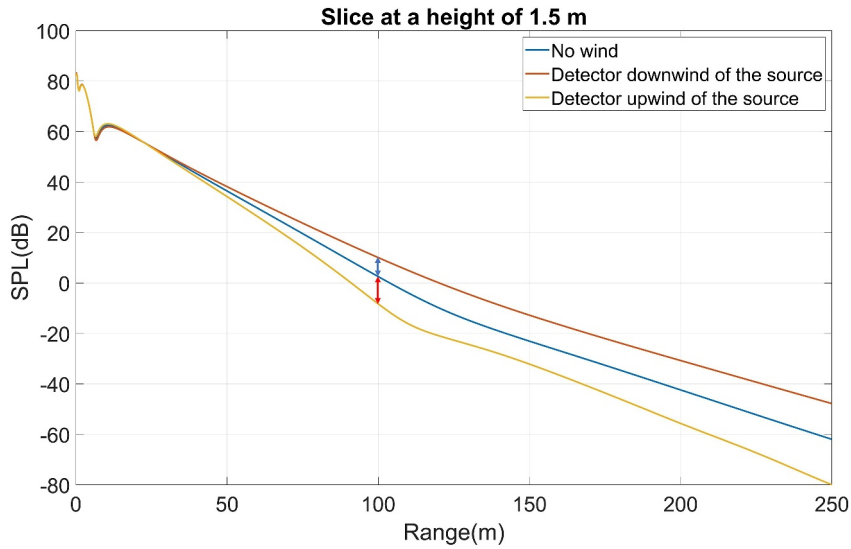


**Figure 13.** The sound pressure level extracted from the PE simulation presented in Figure 12 at a height of 1.5 m plotted as a function of the horizontal distance from the source (horizontal slices of PE simulations). Blue line: extracted from the simulation with no wind, Figure 12b. Red line: extracted from the simulation for which the detector is downwind of the source, Figure 12a. Yellow line: extracted from the simulation for which the detector is upwind of the source, Figure 12c.

this increase of ground temperature is smaller than the effect of changing the ground type, with a maximum decrease in SPL outside the interference patterns of 0.5 dB.

To summarize, the effect of the ground on sound propagation consists mainly of the creation of interference patterns, whose location and depth is determined by the sound frequency and the ground impedance. Ground impedance is sensitive partly to the pressure and temperature at the ground level but mostly to the material structural parameters (grain size and porosity). This means that, if every relevant meteorological variables are precisely known, the knowledge of the interference patterns position could help to place constraints on the ground properties. However, the effects of the variation of the ground impedance on the magnitude of the sound field outside the interference patterns is small compared to every other effects that are investigated in the following sections.

### 3.2. Effect of the Temperature Profile

Ground-based measurements of the Martian temperature profile (Munguira et al., 2023; M. D. Smith et al., 2006) have shown that it presents a consistent diurnal pattern, with a stable stratified atmosphere during the night and a strong super-adiabatic vertical gradient from mid-morning to mid-afternoon. Because the speed of sound increases with temperature, this gradient translates into a sound speed gradient. This causes refraction of the sound

**Table 4**
*Different Values for the Standard Deviation of Temperature and Wind Speed Fluctuations at Noon*

| | | Altitude(m) | | |
|---|---|---|---|---|
| Parameter | Source | 0.5 | 1.45 | 10 |
| Temperature fluctuations standard deviation(K) | In situ (Mars 2020) | – | 1.5–4 | – |
| | Similarity theory | 2.3 | 2.0 | 1.3 |
| Wind speed fluctuations standard deviation(m/s) | In situ (Mars 2020) | – | 1–3 | – |
| | Similarity theory | 2.2 | 2.2 | 2.2 |

*Note*. In situ measurement are for Jezero crater at noon and can be found in Munguira et al. (2023) for the temperature and Viúdez-Moreiras, Lemmon et al. (2022) for the wind speed. They correspond to the standard deviation of the air temperature (respectively wind speed) on a 5 min windows.



21699100, 2024, 7, Downloaded from https://agupubs.onlinelibrary.wiley.com/doi/10.1029/2024JE008469 by Cochrane France, Wiley Online Library on [12/12/2024]. See the Terms and Conditions (https://onlinelibrary.wiley.com/terms-and-conditions) on Wiley Online Library for rules of use; OA articles are governed by the applicable Creative Commons License

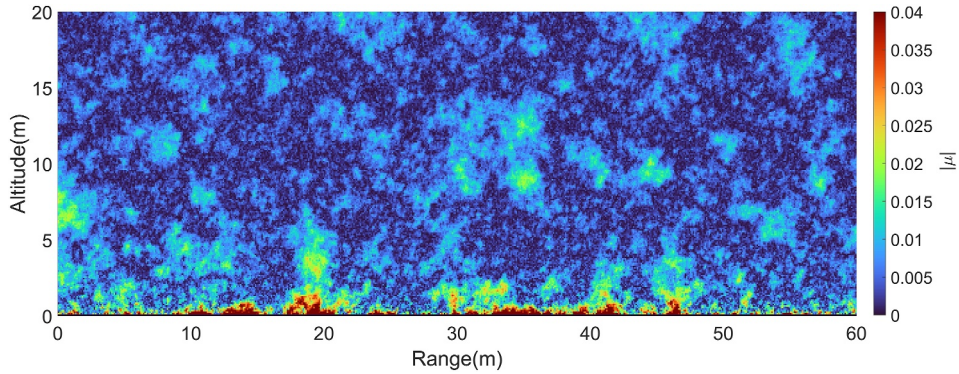


**Figure 14.** Modeled field of $\mu$, the refractive index fluctuation near Perseverance site at 12 LTST. The color scale corresponds to the absolute value of the refractive index at each point of the range-altitude plane. The turbulence is inhomogeneous, with turbulent parameters obtained by scaling similarity theory results to the upper bound of the standard deviation measurement given in Table 4 (i.e., 4 K and 3 m/s). Note that while the color bar is limited to 4% so that smaller variation are visible, the actual maximal $\mu$ attained in the bottom layer of the atmosphere is 6%.

waves, which are bent toward the low-speed of sound area. The goal of this section is to quantify the change in the sound field induced by this refraction.

Figure 7 illustrates sound refraction with a simple ray tracing model, where rays are propagated in straight lines across layers. Each layer has a different speed of sound, and the ray's direction is changed following Snell's Law each time a ray crosses an interface between two layers. The ray paths are simulated over an air temperature profile from the MCD at Perseverance site at a solar longitude of 180° taken at 10 cm increments. The source is located 3 m above the ground.

Figure 7 shows that while at 6 LTST the sound is propagating in all directions, at 12 LTST there is an area close to the ground where there is no ray. This effect, well-known in atmospheric acoustics as well as in other disciplines, is referred to as a shadow zone. To quantify the impact of the shadow zone, we have propagated sound waves in both a refractive and a homogeneous atmosphere, following the process described in Section 2. Atmospheric turbulence is not included in these simulations. As these two types of profile occur at different times of day, and thus at different average air temperatures, it is not meaningful to isolate the effect of the temperature profile from the effect of the average temperature by comparing two Martian atmospheres. As a result, the first profile we used

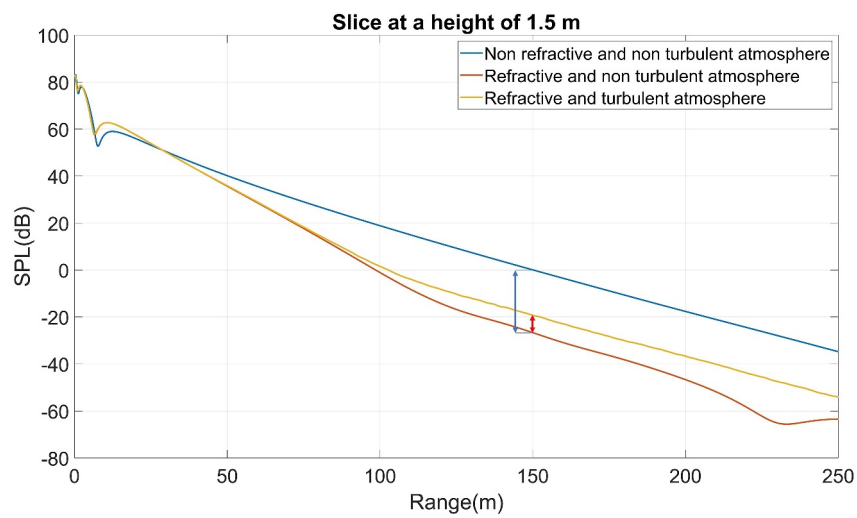


**Figure 15.** Sound pressure level extracted from PE simulations with and without atmospheric turbulence, at a height of 1.5 m plotted as a function of the distance from the source. The result of the turbulent simulation are obtained by averaging 100 iterations (see Section 2.5). The source is 3 m above the ground.



21699100, 2024, 7, Downloaded from https://agupubs.onlinelibrary.wiley.com/doi/10.1029/2024JE008469 by Cochrane France, Wiley Online Library on [12/12/2024]. See the Terms and Conditions (https://onlinelibrary.wiley.com/terms-and-conditions) on Wiley Online Library for rules of use; OA articles are governed by the applicable Creative Commons License

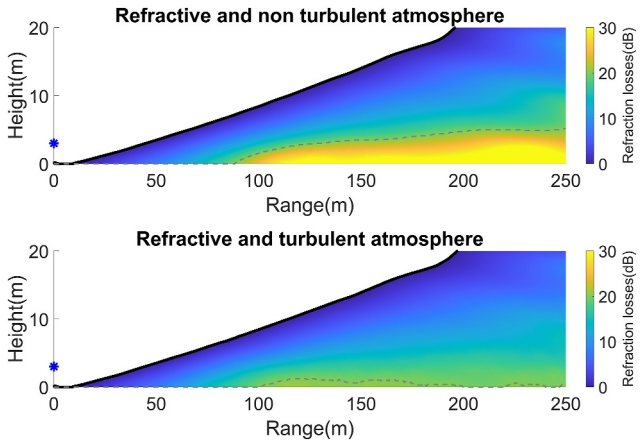


**Figure 16.** Comparison of the depth of the shadow zone for a non-turbulent and a turbulent atmosphere. Top: shadow zone depth in the case of a refractive atmosphere with the detector upwind of the source. Bottom: same atmosphere with the addition of atmospheric turbulence shown in Figure 14. For the meaning of the color scale see Figure 10 caption. The dashed line defines the zone where the losses are greater than 20 dB. The blue star is the sound source.

is not from the MCD but is a hot and homogeneous atmosphere, which was obtained by averaging over the altitude the simulation of the MCD at 12 LTST. The second one is a hot and refractive atmosphere that corresponds to the simulation of the MCD at 12 LTST.

Figure 8 shows the results of the PE method for the homogeneous and the refractive atmospheres. The temperature profile that was used to compute the speed of sound is displayed on the left. The interference patterns created by reflection on the ground presented in Section 3.1 are still present. An upward bending is visible in the refractive atmosphere. This results in the creation of a low SPL shadow zone close to the ground. The effect of sound refraction can be seen by comparing the hot and homogeneous atmosphere (Figure 8 top) and the hot and refractive one (Figure 8 bottom). Figure 9 presents the same simulations as Figure 8 but only at the height of 1.5 m. This can simulate for example, the SPL received by a ground based microphone as it is going away from the sound source. Data from a simulation at 6 LTST at the Perseverance site, which corresponds to a cold and homogeneous atmosphere, has also been added for comparison with the effect of the diurnal cycle of temperature.

Figure 9 shows that for the same sound source, the received sound at 100 m would be 30 dB lower at 12 LTST, when the atmosphere is hot and refractive, than at 6 LTST, when it is cold and homogeneous. The comparison of sound level with the hot and homogeneous atmosphere shows that of these 30 dB of excess losses, 15 dB are due to the higher attenuation and 15 dB to the sound refraction. Acoustic losses due to refraction are thus of the same order of magnitude than those due to the increase of the attenuation coefficient and are not to be ignored when modeling sound propagation on the Martian surface. It also shows that the position of the interference patterns at a range of 10 m is very slightly changed with sound refraction.

The shadow zone is defined as the area close to the ground where the SPL is lower because of the refraction. We can thus define an upper boundary of the shadow zone, which is the altitude under which the SPL in the refractive case is lower than the SPL in the non-refractive case. We can also define the shadow zone depth as the difference between the SPL in the refractive case and the SPL in the non-refractive case in the shadow zone. This

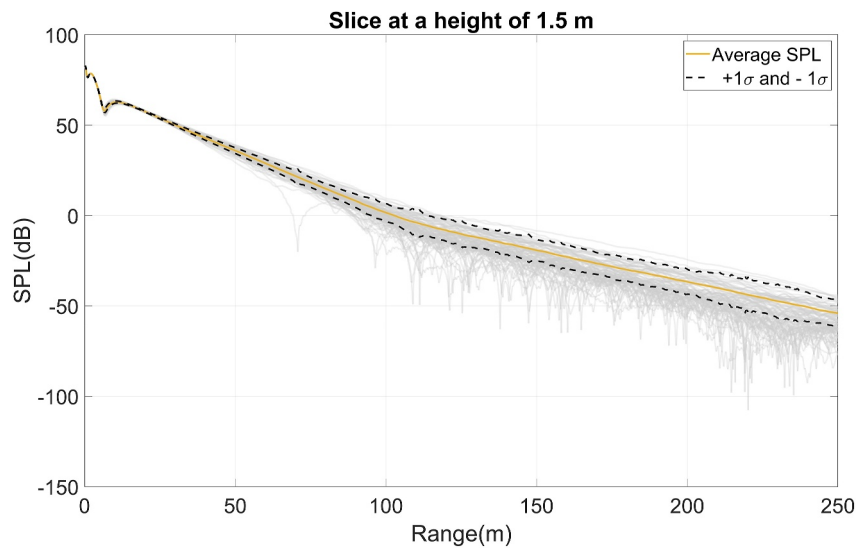


**Figure 17.** Sound pressure levels extracted from PE simulations at a height of 1.5 m. The PE simulations are the ones that were used to compute the "refractive and turbulent atmosphere" of Figure 15. Each gray line correspond to one of the 100 realizations with a specific $\mu$ field (see Section 2.5). The yellow line is the average of all the realization. The dashed lines show the standard deviation of the all the SPL.



21699100, 2024, 7, Downloaded from https://agupubs.onlinelibrary.wiley.com/doi/10.1029/2024JE008469 by Cochrane France, Wiley Online Library on [12/12/2024]. See the Terms and Conditions (https://onlinelibrary.wiley.com/terms-and-conditions) on Wiley Online Library for rules of use; OA articles are governed by the applicable Creative Commons License

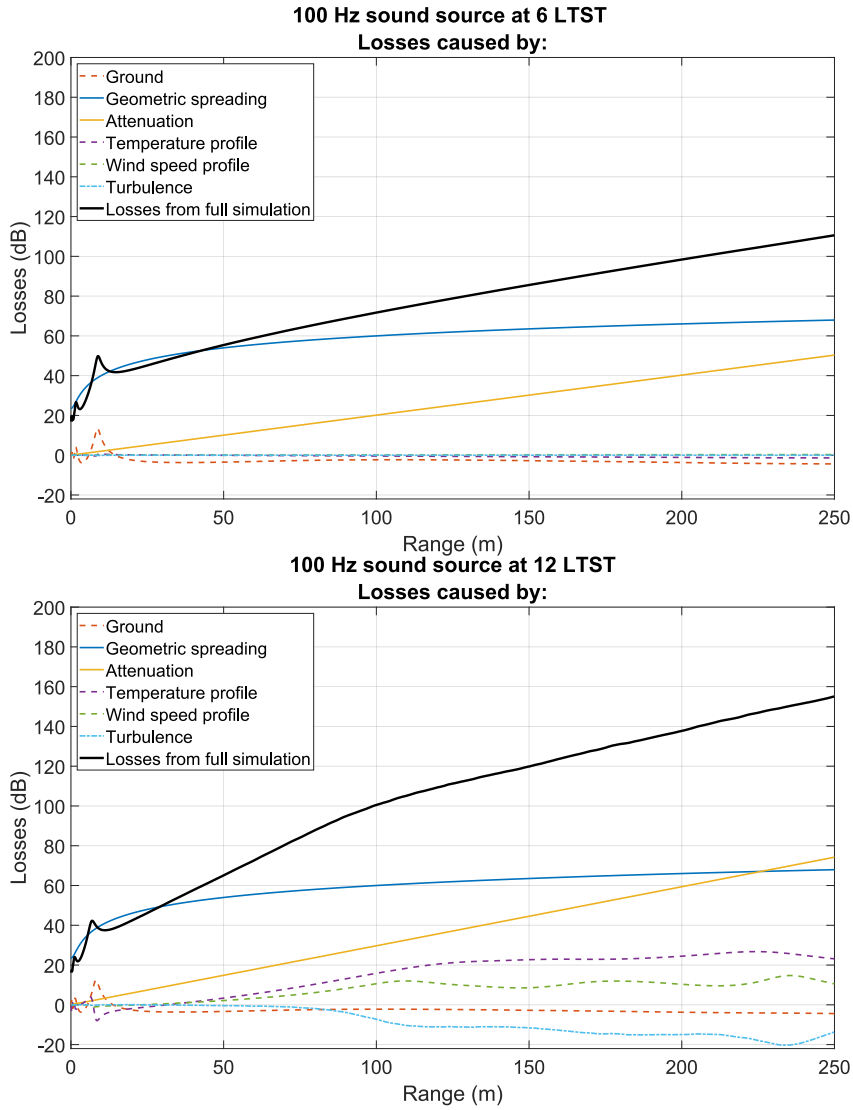


**Figure 18.** Acoustic losses in dB for a 100 Hz sound wave as a function of range at 6 LTST and 12 LTST. The different colored lines show the losses associated with each causes. The black lines show the losses associated with a simulation that take into account all the loss causes. All simulations were made using the atmosphere at Perseverance site at a solar longitude of 180°. Losses are counted positively, a negative loss correspond to a gain of SPL. For the wind profile, the detector is upwind of the source. The peaks and dips close to the source correspond to interference patterns.

corresponds to the additional losses induced by sound refraction. A complete representation of the depth of the shadow zone can be seen in Figure 10.

Figure 10 shows that the losses due to refraction are stronger near the ground and far away from the source. To have a better idea of the importance of these losses at the Martian surface, we have simulated propagation of sound in the Earth atmosphere near the ground using a temperature profile measured in the Egyptian desert in July at 1 p.m. (Flower, 1937; Geiger et al., 1995) when the temperature gradient is the strongest. The temperature gradient in these conditions is nonetheless very small compared to Martian conditions, with a difference of temperature between the ground and 2 m high of only around 4 K compared to around 40 K near the Martian surface.

Figure 11 shows that as a result of this weaker temperature gradient, not only the extent of the shadow zone is smaller on Earth, but the associated losses in SPL are also around 10 times smaller with a maximum of 3 dB.



21699100, 2024, 7, Downloaded from https://agupubs.onlinelibrary.wiley.com/doi/10.1029/2024JE008469 by Cochrane France, Wiley Online Library on [12/12/2024]. See the Terms and Conditions (https://onlinelibrary.wiley.com/terms-and-conditions) on Wiley Online Library for rules of use; OA articles are governed by the applicable Creative Commons License

**Table 5**
*A Summary of All the Features of the Martian Surface That Have an Impact on the Sound Level Created by a Specific Sound Source, Expressed in dB or in Change in the Attenuation Coefficient α*

| Feature of the Martian surface | | Impact on the sound fields |
|---|---|---|
| Variation of the ground impedance with | The temperature | Very small (∼0.5 dB)[a] |
| | The grain size | Small (∼2 dB)[a] |
| Seasonal cycle of | Pressure and $CO_2$ | Small (up to ∼10% of $\alpha$ at high Latitude)[b] |
| | Temperature | Medium (up to ∼75% of $\alpha$ at high latitude)[b] |
| Diurnal cycle | Of temperature | Large ($\alpha \times 2$–3)[b] |
| Refraction caused by | The temperature profile | Large (from −15 to +3 dB at 100 m depending on time of day)[a] |
| | The wind profile | Large (from −11 to +7 dB at 100 m depending on direction)[a] |
| Atmospheric | Turbulence | Medium (+5 dB at 150 m)[a] |

[a]In the configuration presented in this work: a 100 Hz sound source 3 m above the ground with a receiver at 1.5 m from the ground. [b]For a 100 Hz soundwaves, see Gillier et al. (2024).

In summary, the vertical gradient of temperature that occurs near the Martian surface during the middle of the day leads to refraction of sound waves and thus the creation of a low SPL area near the ground, known as the shadow zone. Given the magnitude of the temperature gradient near the Martian surface, this effect is an order of magnitude stronger than on Earth. It is also of the same order of magnitude that the losses induced by the increase of the acoustic attenuation coefficient because of the rise in temperature between sunrise and midday on Mars.

### 3.3. The Effect of the Wind Velocity Profile

In windy conditions, the effective speed of sound $c_{eff}$ will be the composition of the thermal speed of sound $c$ and the projection of the horizontal wind speed on the direction of the sound propagation $u \cos \theta$. Because of the drag at the ground, wind generally increases with altitude over the first tens of meters from the surface. Wind speed usually presents a logarithmic profile with a strong vertical gradient close to the ground. Therefore, if the wind direction is from the detector to the source, it will create a negative gradient of effective sound speed. As mentioned in Section 3.2 it will refract the sound upward and thus diminish the acoustic intensity close to the ground by creating a shadow zone. On the contrary, if the wind direction is from the source toward the detector it will create a positive gradient of effective sound speed, thus causing downward refraction of the sound and

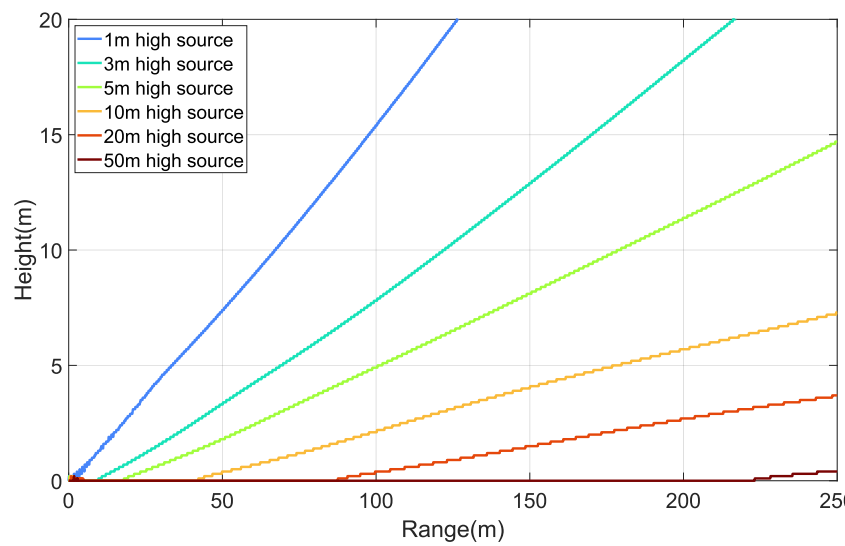


**Figure 19.** The upper boundary of the shadow zone for a sound source located between 1 and 50 m above the ground. Each colored lines corresponds to the upper boundary of a shadow zone (see Figure 10) for a source at a specific altitude. The simulation is done for a 100 Hz source at 12 LTST. The wind is blowing from the microphone toward the sound source and has a speed of 4 m/s at 1.5 m above the ground.



21699100, 2024, 7, Downloaded from https://agupubs.onlinelibrary.wiley.com/doi/10.1029/2024JE008469 by Cochrane France, Wiley Online Library on [12/12/2024]. See the Terms and Conditions (https://onlinelibrary.wiley.com/terms-and-conditions) on Wiley Online Library for rules of use; OA articles are governed by the applicable Creative Commons License

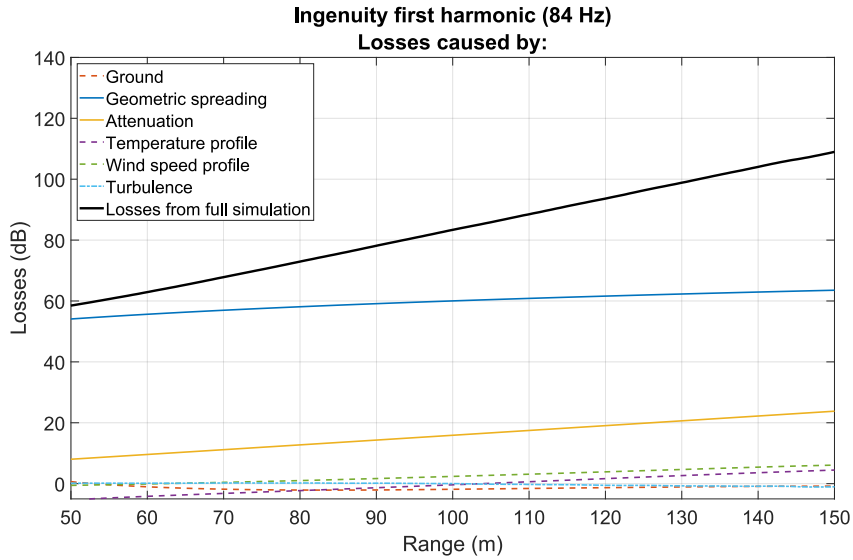


**Figure 20.** Simulation of an Ingenuity flight. The different colored lines show the losses associated with each causes. The black lines show the losses associated with a simulation that take into account all the loss causes. The sound source is 10 m above the ground, the microphone is 2.1 m above the ground. The microphone is upwind of the source. The atmosphere is the one at Perseverance site at 12 LTST and Ls = 180°.

increasing the near-ground intensity. In situ measurements (Newman et al., 2022; Viúdez-Moreiras, Lemmon, et al., 2022) have shown that, while the wind patterns depend on the local topography and the wind speed exhibits high short term variability, wind is generally stronger during daytime than at night. Thus, it will be during the middle of the day that the effect of wind will be stronger.

Figure 12 illustrates the effect of the wind on the sound propagation. It consists of the result of a PE simulation for which the atmospheric parameters are extracted from the MCD at a local time of 12 LTST as this is the time when the wind is the strongest, and it allows comparison with the simulations of Section 3.2. We use a wind speed profile scaled to 4 m/s at 1.5 m in line with the wind speeds observed by Perseverance in Viúdez-Moreiras, Lemmon, et al. (2022). Turbulence is not included in these simulations.

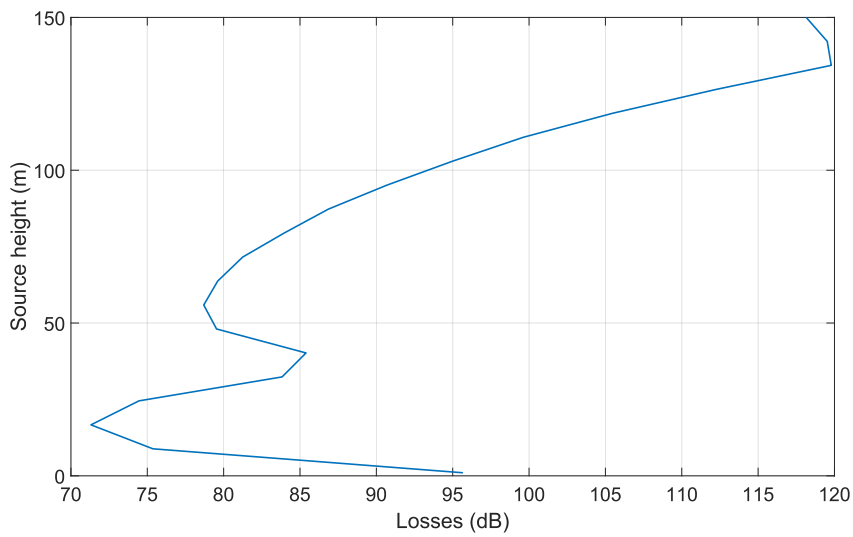


**Figure 21.** Losses for a 100 Hz source at different altitude. The microphone is situated 80 m from the source landing site at 2.1 m above the ground. The atmosphere used for the simulations is the same as in Section 3.5 that is, Perseverance site at Ls = 180 and 12 LTST with the microphone upwind of the source.



21699100, 2024, 7, Downloaded from https://agupubs.onlinelibrary.wiley.com/doi/10.1029/2024JE008469 by Cochrane France, Wiley Online Library on [12/12/2024]. See the Terms and Conditions (https://onlinelibrary.wiley.com/terms-and-conditions) on Wiley Online Library for rules of use; OA articles are governed by the applicable Creative Commons License

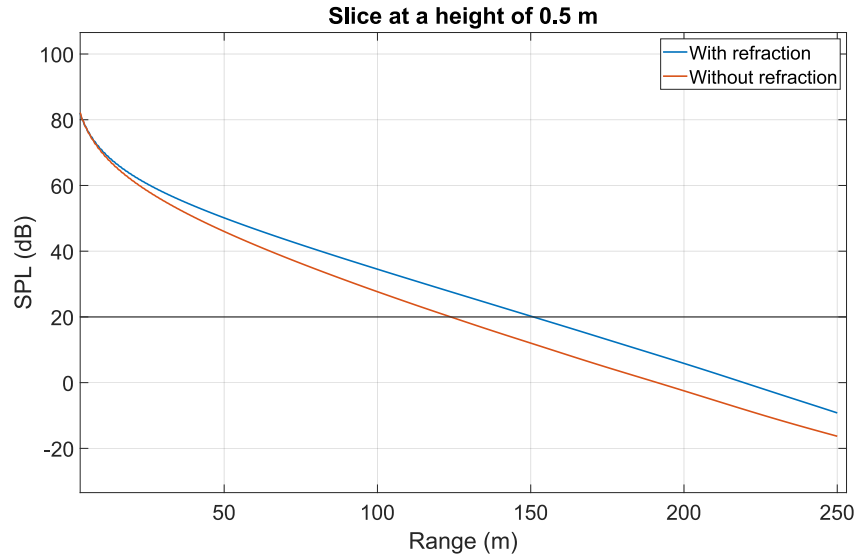


**Figure 22.** Comparison of the SPL 0.5 m above the ground. The with refraction curve correspond to an atmosphere is extracted from the MCD at Perseverance site at 0 LTST. The detector is downwind of the source, with a wind speed of 4 m/s at 1.5 m above the ground. The sound source is 0.5 m above the ground. The without refraction curve correspond to the same situation with a constant temperature and wind speed profile.

When the detector is downwind of the source (positive wind speed) the shadow zone close to the ground is smaller, whereas when the detector is upwind of the source (negative wind speed) it is larger. To quantify this effect we can look at the sound amplitude at 1.5 m high as a function of the distance from the source shown in Figure 13. At 100 m from the source, the variation in the SPL induced by the change in refraction caused by the wind vertical gradient can go from −11 to +7 dB. This means that the variations in sound amplitude created by the wind are of the same order of magnitude than the ones created by the vertical gradient of temperature or the diurnal variation of temperature, and thus cannot be ignored.

In summary, the wind speed profile near the Martian surface create sound refraction, which can leads to an increase or a decrease of the SPL near the ground depending on the wind direction.

### 3.4. The Effect of Atmospheric Turbulence

The wind speed and the temperature at the surface of Mars exhibit short term fluctuations. These turbulent fluctuations follow a diurnal cycle (Petrosyan et al., 2011). During the day, the temperature difference between the hot surface and the colder atmosphere leads to the creation of ascending thermal plumes. The turbulence is thus buoyancy-driven. At night, the radiative cooling of the ground leads to a stably stratified atmosphere, where the turbulence is weaker and created mainly by wind shear. Wind speed and temperature fluctuation are thus smaller during nighttime. In this section we will focus on the Martian atmosphere at 12 LTST as it is the time of day when the turbulent fluctuations in both temperature and wind speed are at their maximum (Munguira et al., 2023; Stott et al., 2023; Viúdez-Moreiras, de la Torre, et al., 2022).

The first step to simulate the effects of atmospheric turbulence on the sound field is to compute the turbulent parameters as shown in Section 2.5. In Table 4 we compare the values estimated using the similarity relations proposed in V. E. Ostashev (2016) (see Equations B2–B7) to the ones measured by MEDA, the meteorological package of the Perseverance rover. The values derived using similarity theory are computed based on data from the MCD at the Perseverance site at noon, so they can be compared to MEDA data. Table 4 shows that they are consistent with the in situ measurements.

Figure 14 shows an example of a field of $\mu$, the refractive index fluctuation, near Perseverance site at 12 LTST and thus represents one of the many instances of turbulent fields which are used to simulate the effects of turbulence. It was obtained by scaling the standard deviations profiles given by the similarity relations so that they are equal to the upper bound of the measured one at 1.45 m (i.e., 4 K and 3 m/s). It thus represents a case of intense turbulence, with



21699100, 2024, 7, Downloaded from https://agupubs.onlinelibrary.wiley.com/doi/10.1029/2024JE008469 by Cochrane France, Wiley Online Library on [12/12/2024]. See the Terms and Conditions (https://onlinelibrary.wiley.com/terms-and-conditions) on Wiley Online Library for rules of use; OA articles are governed by the applicable Creative Commons License

21699100, 2024, 7, Downloaded from https://agupubs.onlinelibrary.wiley.com/doi/10.1029/2024JE008469 by Cochrane France, Wiley Online Library on [12/12/2024]. See the Terms and Conditions (https://onlinelibrary.wiley.com/terms-and-conditions) on Wiley Online Library for rules of use; OA articles are governed by the applicable Creative Commons License

$\mu$ stronger close to the ground. In this case, in can go up to 0.06, which mean that locally the value of the speed of sound can be as much as 6% different from the average value over time. Only the first 60 m of range are shown to preserve the figure aspect ratio. One must keep in mind that given the large uncertainties of the turbulent parameters at the surface of Mars, this is merely an example of what could exist on Mars.

Figure 15 presents the results of PE simulations computed using the type of $\mu$ fields presented in Figure 14 for a 100 Hz source. To keep this mostly illustrative section short, the difference of turbulence effect for different frequency is not analyzed here. The case of a non-refractive atmosphere and of a refractive but non-turbulent atmosphere were also plotted for reference. This demonstrates that the first effect of turbulence is to "make sound leak" into the shadow zone. This is a well-known effect of atmospheric turbulence on Earth. For example, at a range of 150 m the SPL in the case of turbulence is at best 5 dB higher than in the non-turbulent case. Given that at this range the difference between the non-refractive case and the refractive case (the depth of the shadow zone) is 25 dB, it means that turbulence is capable of making up for one fifth of the shadow zone losses in terms of SPL or is able to nearly double the pressure amplitude. However, turbulence has no impact on the extent of the shadow zone, only on its depth, as shown in Figure 16. This has the effect of reducing areas of significant losses, for example, the area where refractive losses are greater than 20 dB, has almost disappeared.

The second effect of the turbulence is to remove the interference patterns, as shown with the interference minimum that occurs at a range of 230 m in Figure 15 in the non-turbulent atmosphere but has disappeared in the turbulent cases.

These results are the average of one hundred simulation and represent an average of the SPL over a few minutes period. However, fluctuation in SPL are also interesting. Figure 17 illustrate these fluctuations with the same PE simulation that is displayed in Figure 15. In this figure, in addition to the average SPL, all individual realizations are plotted as well as their standard deviation. It shows that the interference patterns for each individual realization are not necessarily located at a range of 230. In fact, there can be multiple minima located anywhere along the range axis or no minimum at all. It is therefore the averaging that is responsible for the removing of the interference patterns.

In summary, the turbulent fluctuations of the temperature and the wind speed near the ground are responsible for a decrease in the depth of the interference patterns and the shadow zone. While the uncertainties on the characteristic of atmospheric turbulence at the Martian surface prevent us from asserting with confidence the magnitude of this effect, our best estimation from our simulations is that it is making up for around one fifth of the refraction losses.

### 3.5. Summary

Figure 18 presents a more detailed view of the different factors that affect sound propagation. It shows the losses in SPL that would be experienced by a 100 Hz sound wave traveling through the Martian atmosphere at 6 LTST and at 12 LTST. Losses are broken down by causes. All the causes are assumed to be independent of one another when evaluating their effect. Hence, the geometric spreading is computed by multiplying the sound amplitude by $\frac{1}{r}$, the attenuation by multiplying the sound amplitude by $\exp(-\alpha r)$ where $\alpha$ is the attenuation coefficient (Gillier et al., 2024), the losses caused by the ground, the temperature profile, the wind speed profile and turbulence are computed by subtracting a PE simulation with the relevant phenomenon to a PE simulation without. The losses obtained by simulating all the causes simultaneously (the full simulation) is also displayed.

Figure 18 shows that, at 100 Hz, the dominant cause of acoustic losses is the geometrical spreading, followed by attenuation. At 12 LTST losses caused by the refraction (temperature profile and wind speed) grow with distance and turbulence can only make up for a fraction of these losses. The sum of all losses is not displayed in the figures but is very closed to the losses from the full simulation. The fact that at 6 LTST the attenuation is smaller, the temperature gradient is positive and thus causes small acoustic gains and the wind is weaker, make this time of day the most acoustically favorable. Table 5 presents a more general summary of all the features of the Martian surface that have an impact on the sound level created by a specific sound source based on Gillier et al. (2024) and this work.

21699100, 2024, 7, Downloaded from https://agupubs.onlinelibrary.wiley.com/doi/10.1029/2024JE008469 by Cochrane France, Wiley Online Library on [12/12/2024]. See the Terms and Conditions (https://onlinelibrary.wiley.com/terms-and-conditions) on Wiley Online Library for rules of use; OA articles are governed by the applicable Creative Commons License

## 4. Applications

In this section, the model is used to simulate two application cases, the flight of the Ingenuity helicopter and the detection of a descending sound source. The effect of the altitude of the source on the refractive shadow zone, which is relevant to both cases, is first briefly discussed. We also look at how much can refraction improve the propagation distance of a sound wave at the surface of Mars.

### 4.1. Effect of the Height of the Source

The size of the shadow zone not only depends on how refractive is the atmosphere, that is, how strong is the vertical temperature and wind speed gradient, but is also strongly dependent on the height of the sound source, as illustrated in Figure 19 representing the extent of the shadow zone at 12 LTST. The wind is blowing from the microphone toward the sound source and has a speed of 4 m/s at 1.5 m above the ground. The effects of atmospheric turbulence are neglected. It shows that the size of the shadow zone is greater when the source is closer to ground and conversely there is a source altitude above which the shadow zone disappears.

### 4.2. Ingenuity Flight

One of the sound sources that was recorded at the Martian surface by the SuperCam microphone is that of the helicopter Ingenuity (Lorenz et al., 2023). The helicopter mostly flies at an altitude of 10 m, while the SuperCam microphone is located 2.1 m above the ground. The helicopter never goes closer than 50 m to the rover, and Perseverance microphone was not able to hear it farther than 150 m. All the recorded flights have taken place around noon. Figure 20 presents a simulation of sound propagation from the helicopter to the SuperCam microphone during a flight, with a breakdown of the losses by their causes. It shows that, because of the relatively high altitude of the source, the losses caused by refraction are very small compared to the geometric spreading and the atmospheric attenuation. This means that when deriving the value of the atmospheric attenuation coefficient from Ingenuity received sound amplitude, one can neglect refraction, as was done in Chide et al. (2023).

### 4.3. Descending Source

An interesting case to consider is the one of a sound source landing close to the microphone. This could simulate, for example, the landing of the Mars Sample Return mission close to Perseverance rover. Figure 21 presents such a simulation for a sound source landing 80 m away from the microphone at noon. This is of course a distance way too small to be realistic, but the following also apply for longer distances.

It shows that in the first phase of the descent, loses are diminishing as the source is getting closer to the microphone except when it crosses an interference minimum, which is the case for example, at 40 m high in this example. However, when the source is sufficiently close to the ground, the refraction losses are increasing as the source is getting close to the ground. This is not compensated by the shorter distance, and thus the received sound is diminishing. In the example presented in Figure 21 this effect is so strong that the losses are equivalent when the source at the surface and 100 m above the ground. This effect would be weaker if the atmosphere was less refractive, for example, with a landing early in the morning, or if the microphone was closer to the landing site.

### 4.4. Propagation Enhanced by Refraction

In this paper, we have focused on the losses induced by the refraction of sound, as they are considerable during the day. However, during the night the temperature profile is inverted, with the temperature at the ground level typically a few Kelvin under the temperature at 2 m above the ground. Thus, if a sound wave is traveling with the wind at this time of day, the sound will be refracted toward the ground; in this case sound propagation near the ground in enhanced by refraction. To quantify this effect, we have simulated the best possible case regarding refraction. The atmosphere is extracted from the MCD at Perseverance site at 0 LTST, as it is the time of day when the temperature gradient is most positive in the MCD. It must be noted, however, that the precise time of day when the gradient is the strongest can vary with the season, the terrain of the atmosphere dust content. The detector is downwind of the source with a wind speed of 4 m/s at 1.5 m above the ground, which is very high for this time of day. The sound source is very close to the ground, at 0.5 m high. Figure 22 shows the result of this simulation as well as the same simulation with no refractive effect to assess the impact of temperature and wind induced refraction. If we assume a detectability threshold of 20 dB for a receptor, Figure 22 demonstrates that the

effect of refraction on the sound propagation is to increase the maximal distance at which the sound source can be detected from 125 to 150 m. Thus, even in the best case scenario, downward refraction can not significantly enhance sound propagation: there are no acoustic waveguides near the Martian surface.

## 5. Conclusion

The model presented in this work can be used to simulate propagation of sound waves near the Martian surface at any location, any time of year and any time of day. It shows that the presence of the ground leads to a slight increase in the SPL field and the creation of interference patterns. The variations of the ground acoustic impedance, with ground properties or temperature, have a small impact on the sound field compared to the other phenomenon discussed here, but are important to predict the location of the interference patterns. The strong thermal gradient near the surface around noon leads to the creation of a low sound pressure level zone near the ground: the shadow zone. The SPL losses induced in this thermal driven shadow zone are very strong: they are of the same order of magnitude than the ones that come from the diurnal variation of the attenuation coefficient (Gillier et al., 2024) and one order of magnitude stronger than what is typical on Earth. The wind profile can enhance the shadow zone if the detector is upwind of the source, and diminish it if the detector is downwind of the source. The SPL losses induced in this wind driven shadow zone are of the same order of magnitude than what is observed on Earth. The turbulent fluctuations of the temperature and the wind speed can allow the sound to leak into the shadow zone. At the maximum time of turbulence, around noon, this effect can make up to one fifth of the shadow zone. Atmospheric turbulence also removes the interference patterns. The refractive effects are rapidly diminishing with the height of the sound source: in a configuration with the source 10 m above the ground, for example, a flight of the Ingenuity helicopter, they are already negligible.

Such a model could be to better estimate the absolute sound intensity of the Ingenuity rotorcraft (Lorenz et al., 2023) and compare it with results given by aeroacoustic models of rotorcraft (Hanson, 1985). In the future, the model could be improved, particularly by using better estimation of the ground parameter and the turbulent spectrum or by including the effect of the terrain irregularity. Finally, this kind of model can be relatively easily adapted to sound propagation at the surface of other planetary bodies especially Venus and Titan.

## Appendix A: Coefficients for the von Kármán Spectral Density

The following numerical constant, used in Equation 5 are valid for every spectral density of the von Kármán type.

$$B_1 = \frac{A\Gamma(1/2)\Gamma(8/6)}{4\Gamma(11/6)} \tag{A1}$$

$$B_2 = \frac{22A\Gamma(3/2)\Gamma(8/6)}{12\Gamma(17/6)} \tag{A2}$$

$$B_3 = \frac{22A\Gamma(1/2)\Gamma(14/6)}{12\Gamma(17/6)} \tag{A3}$$

with $A = 0.033$ and $\Gamma$ the gamma function.

## Appendix B: Derivation of the Turbulent Parameters

This section explains how to compute the standard deviation of the turbulent fluctuations of temperature, $\sigma_T$ and wind speed, $\sigma_v$ as well as their length scale $L_T$ and $L_v$ with the method described in V. E. Ostashev (2016).

### B1. The Monin-Obukhov Similarity Theory Parameters

According to Monin-Obukhov similarity theory (MOST) when correctly normalized the standard deviation and length scale are a function of $z/L_o$, where z is the altitude and $L_o$ the Obukhov length:



21699100, 2024, 7, Downloaded from https://agupubs.onlinelibrary.wiley.com/doi/10.1029/2024JE008469 by Cochrane France, Wiley Online Library on [12/12/2024]. See the Terms and Conditions (https://onlinelibrary.wiley.com/terms-and-conditions) on Wiley Online Library for rules of use; OA articles are governed by the applicable Creative Commons License

$$L_o = -\frac{u_*^3 T_s}{\kappa_v g \left(\overline{w'T'}\right)_s} \tag{B1}$$

with $u_*$ the friction velocity, $T_s$ the temperature of the surface, $\kappa_v$ the von Kármán constant, usually taken at 0.4, g the surface gravity acceleration, equal to 3.71 m/s$^2$ on Mars and $\left(\overline{w'T'}\right)_s = -u_* T_*$ the kinematic heat flux at the surface with $T_*$ the temperature scale.

Because MOST predicts that the wind speed and temperature profiles are proportional to the product of $u_*$ (respectively $T_*$), times the logarithm of the altitude, it is possible to derive $u_*$ (respectively $T_*$) from the value of wind speed (respectively temperature) at two heights or more. These values can be extracted from the MCD or from in situ measurement when available.

### B2. Similarity Relations for the Turbulent Parameters

Following MOST, some similarity relations on $\sigma_T$, $\sigma_v$, $L_T$, and $L_v$ have been proposed.

The subsequent expressions were obtained in V. Ostashev and Wilson (2000) for the temperature:

$$\frac{\sigma_T^2(z)}{T_*^2} = \frac{4.0}{[1 + 10(-z/L_0)]^{2/3}}, \tag{B2}$$

$$\frac{L_t(z)}{z} = 2.0 \frac{1 + 7.0(-z/L_0)}{1 + 10(-z/L_0)}, \tag{B3}$$

For the wind speed, in the case of shear surface-layer turbulence, the following expression is derived in Wilson (2000):

$$\frac{\sigma_s^2}{u_*^2} = 3.0, \tag{B4}$$

$$\frac{L_s}{z} = 1.8 \tag{B5}$$

and for mixed-layer similarity, when buoyancy is driving the atmospheric turbulence:

$$\frac{\sigma_b^2}{w_*^2} = 0.35, \tag{B6}$$

$$\frac{L_b}{z_i} = 0.23 \tag{B7}$$

with $z_i$ the height of the capping inversion and $w_* = \left[z_i g \left(\overline{w'T'}\right)_s / T_s\right]^{1/3}$ the mixed layer velocity scale. When both shear and buoyancy play a role in generating the wind speed turbulent fluctuations, the standard deviations and length scales can be combined as shown in Wilson (2000):

$$\sigma_v^2 = \sigma_s^2 + \sigma_b^2 \tag{B8}$$

$$\frac{\sigma^2}{L_v^{p-1}} = \frac{\sigma_s^2}{L_s^{p-1}} + \frac{\sigma_b^2}{L_b^{p-1}} \tag{B9}$$

with $p = \frac{5}{3}$

These expressions are valid for stratifications ranging from unstable to slightly stable.



21699100, 2024, 7, Downloaded from https://agupubs.onlinelibrary.wiley.com/doi/10.1029/2024JE008469 by Cochrane France, Wiley Online Library on [12/12/2024]. See the Terms and Conditions (https://onlinelibrary.wiley.com/terms-and-conditions) on Wiley Online Library for rules of use; OA articles are governed by the applicable Creative Commons License

## Notation

| | |
|---|---|
| $\alpha$ | Attenuation coefficient |
| $\alpha_n$ | Random angle in the random-phase method |
| $\bar{n}$ | Average of the refractive index over time |
| $\Delta r$ | Grid spacing in the range direction in the PE method |
| $\Delta r$ | Grid spacing in the altitude direction in the PE method |
| $\eta$ | Coefficient of shear viscosity |
| $\Gamma$ | Gamma function |
| $\kappa$ | Thermal conductivity |
| $\mu$ | Refractive index turbulent fluctuation |
| $\omega$ | Angular frequency |
| $\phi_m$ | Microporosity in the VBU model |
| $\phi_p$ | Intergranular porosity in the VBU model |
| $\rho$ | Atmospheric density |
| $\sigma_T$ | Standard deviation of the temperature turbulent fluctuations |
| $\sigma_v$ | Standard deviation of the wind speed turbulent fluctuations |
| $\theta$ | Angle between the wind speed direction and the source-microphone line. |
| $\theta_n$ | Random angle in the random-phase method |
| $A_0$ | Pressure received at reference distance |
| $c$ | Speed of sound |
| $c_{eff}$ | Effective speed of sound in the presence of wind |
| $c_0$ | Speed of sound at the temperature $T_0$ |
| $C_p$ | Heat capacity |
| $C_T$ | Structure function parameter of the temperature |
| $C_v$ | Structure function parameter of the wind speed |
| $D_e$ | Nanopore parameter in the VBU model |
| $F$ | Two-dimensional spectral density of the refractive-index fluctuation |
| $H_e$ | Nanopore parameter in the VBU model |
| $k_0$ | Real-part of the wavenumber |
| $K_0$ | Wavenumber representative of the largest eddies |
| $L$ | Size of the largest eddies |
| $L_p$ | Sound pressure level |
| $L_s$ | Solar longitude |
| $L_T$ | Length scale of the temperature turbulent fluctuations |
| $L_v$ | Length scale of the wind speed turbulent fluctuations |
| $n$ | Refractive index |



21699100, 2024, 7, Downloaded from https://agupubs.onlinelibrary.wiley.com/doi/10.1029/2024JE008469 by Cochrane France, Wiley Online Library on [12/12/2024]. See the Terms and Conditions (https://onlinelibrary.wiley.com/terms-and-conditions) on Wiley Online Library for rules of use; OA articles are governed by the applicable Creative Commons License

| | |
|---|---|
| $p$ | Sound pressure fluctuation |
| $P$ | Atmospheric pressure |
| $p_{ref}$ | Reference pressure used to compute the SPL (20 μPa) |
| $r$ | Distance to the sound source |
| $r_m$ | Micropores size in the VBU model |
| $r_p$ | Grain size in the VBU model |
| $T_0$ | Mean temperature of an atmosphere used in a PE simulation. |
| $T_g$ | Ground temperature |
| $u$ | Wind speed |
| $Z$ | Normalized ground impedance ($Z_g/Z_{char}$) |
| $z$ | Altitude |
| $Z_{char}$ | Characteristic acoustic impedance of the air |
| $Z_g$ | Acoustic ground impedance |

## Notation

| | |
|---|---|
| $\kappa_v$ | von Kármán constant |
| $\omega_*$ | Mixed layer velocity scale |
| $\overline{w'T'}$ | Kinematic heat flux at the surface |
| $\sigma_b$ | Standard deviation of the wind speed turbulent fluctuations caused by buoyancy |
| $\sigma_s$ | Standard deviation of the wind speed turbulent fluctuations caused by shear |
| $\sigma_T$ | Standard deviation of the temperature turbulent fluctuations |
| $\sigma_v$ | Standard deviation of the wind speed turbulent fluctuations |
| $g$ | Surface gravity acceleration |
| $L_b$ | Length scale of the wind speed turbulent fluctuations caused by shear buoyancy |
| $L_o$ | Obukhov length |
| $L_s$ | Length scale of the wind speed turbulent fluctuations caused by shear |
| $L_T$ | Length scale of the temperature turbulent fluctuations |
| $L_v$ | Length scale of the wind speed turbulent fluctuations |
| ***Symbol*** | Description |
| $T_*$ | Temperature scale |
| $T_s$ | Temperature at the surface |
| $u_*$ | Friction velocity |
| $z_i$ | Height of the capping inversion |



21699100, 2024, 7, Downloaded from https://agupubs.onlinelibrary.wiley.com/doi/10.1029/2024JE008469 by Cochrane France, Wiley Online Library on [12/12/2024]. See the Terms and Conditions (https://onlinelibrary.wiley.com/terms-and-conditions) on Wiley Online Library for rules of use; OA articles are governed by the applicable Creative Commons License

## Data Availability Statement

The meteorological data from the Martian Climate Database (MCD, Forget et al., 1999; Millour et al., 2018) used as inputs of the model are available at https://www-mars.lmd.jussieu.fr. The code of the model is available in Gillier and Petculescu (2023).

**Acknowledgments**
We gratefully acknowledge funding from the French space agency (CNES), from ISAE-SUPAERO, and from Région Occitanie.

## References

Ainslie, M. A., & Leighton, T. G. (2016). Sonar equations for planetary exploration. *Journal of the Acoustical Society of America*, *140*(2), 1400–1419. https://doi.org/10.1121/1.4960786

Albee, A., Battel, S., Brace, R., Burdick, G., Casani, J., Lavell, J., et al. (2000). Report on the loss of the Mars polar lander and deep space 2 missions.

Bass, H. E., & Chambers, J. P. (2001). Absorption of sound in the Martian atmosphere. *Journal of the Acoustical Society of America*, *109*(6), 3069–3071. https://doi.org/10.1121/1.1365424

Chide, B., Bertrand, T., Lorenz, R. D., Munguira, A., Hueso, R., Sánchez-Lavega, A., et al. (2022). Acoustics reveals short-term air temperature fluctuations near Mars' surface. *Geophysical Research Letters*, *49*(21), e2022GL100333. https://doi.org/10.1029/2022GL100333

Chide, B., Blanc-Benon, P., Bertrand, T., Jacob, X., Lasue, J., Lorenz, R. D., et al. (2024). An acoustic investigation of the near-surface turbulence on Mars. *Journal of the Acoustical Society of America*, *155*(1), 420–435. https://doi.org/10.1121/10.0024347

Chide, B., Jacob, X., Petculescu, A., Lorenz, R. D., Maurice, S., Seel, F., et al. (2023). Measurements of sound propagation in Mars' lower atmosphere. *Earth and Planetary Science Letters*, *615*, 118200. https://doi.org/10.1016/j.epsl.2023.118200

Dallois, L., Blanc-Benon, P., & Juvé, D. (2001). A wide-angle parabolic equation for acoustic waves in inhomogeneous moving media: Applications to atmospheric sound propagation. *Journal of Computational Acoustics*, *9*(02), 477–494. https://doi.org/10.1142/s0218396x01000772

Embleton, T. F. (1996). Tutorial on sound propagation outdoors. *Journal of the Acoustical Society of America*, *100*(1), 31–48. https://doi.org/10.1121/1.415879

Flower, W. D. (1937). An investigation into the variation of the lapse rate of temperature in the atmosphere near the ground at Ismailia, Egypt. *Meteorological Office*.

Forget, F., Hourdin, F., Fournier, R., Hourdin, C., Talagrand, O., Collins, M., et al. (1999). Improved general circulation models of the Martian atmosphere from the surface to above 80 km. *Journal of Geophysical Research*, *104*(E10), 24155–24176. https://doi.org/10.1029/1999JE001025

Geiger, R., Aron, R. H., & Todhunter, P. (1995). *The climate near the ground*. Vieweg+Teubner Verlag. https://doi.org/10.1007/978-3-322-86582-3

Gilbert, K. E., & White, M. J. (1989). Application of the parabolic equation to sound propagation in a refracting atmosphere. *Journal of the Acoustical Society of America*, *85*(2), 630–637. https://doi.org/10.1121/1.397587

Gillier, M., & Petculescu, A. (2023). Acoustic model [Software]. *Zenodo*. https://doi.org/10.5281/zenodo.8188828

Gillier, M., Petculescu, A., Murdoch, N., Stott, A. E., Gerier, S., Maurice, S., & Mimoun, D. (2024). Geographical, seasonal and diurnal variations of acoustic attenuation, and sound speed in the near-surface Martian atmosphere. *Journal of Geophysical Research: Planets*, *129*(5), e2023JE008257. https://doi.org/10.1029/2023je008257

Goetz, W., Pike, W., Hviid, S., Madsen, M. B., Morris, R., Hecht, M., et al. (2010). Microscopy analysis of soils at the Phoenix landing site, Mars: Classification of soil particles and description of their optical and magnetic properties. *Journal of Geophysical Research*, *115*(E8), E00E22. https://doi.org/10.1029/2009JE003437

Hagermann, A., Rosenberg, P., Towner, M., Garry, J., Svedhem, H., Leese, M., et al. (2007). Speed of sound measurements and the methane abundance in Titan's atmosphere. *Icarus*, *189*(2), 538–543. https://doi.org/10.1016/j.icarus.2007.02.004

Hanford, A. D., & Long, L. N. (2009). The direct simulation of acoustics on Earth, Mars, and Titan. *Journal of the Acoustical Society of America*, *125*(2), 640–650. https://doi.org/10.1121/1.3050279

Hanson, D. B. (1985). Noise of counter-rotation propellers. *Journal of Aircraft*, *22*(7), 609–617. https://doi.org/10.2514/3.45173

Ksanfomaliti, L., Goroshkova, N., Naraeva, M., Suvorov, A., Khondryev, V., & Yabrova, L. (1982). Acoustic measurements of the wind velocity at the Venera-13 and Venera-14 landing sites. *Soviet Astronomy Letters*, *8*, 227–229. Translation Pisma v Astronomicheskii Zhurnal, 419-423, 8, 227–229.

Leighton, T., & Petculescu, A. (2008). Sounds in space: The potential uses for acoustics in the exploration of other worlds. *Hydroacoustics*, *11*, 225–239.

Linstrom, P. J., & Mallard, W. G. (2023). *NIST chemistry WebBook, NIST standard reference database number 69*. National Institute of Standards and Technology. https://doi.org/10.18434/T4D303

Lorenz, R. D. (1998). Speed of sound in outer planet atmospheres. *Planetary and Space Science*, *47*(1), 67–77. https://doi.org/10.1016/S0032-0633(98)00099-3

Lorenz, R. D., Maurice, S., Chide, B., Mimoun, D., Stott, A., Murdoch, N., et al. (2023). The sounds of a helicopter on Mars. *Planetary and Space Science*, *230*, 105684. https://doi.org/10.1016/j.pss.2023.105684

Mahaffy, P. R., Webster, C. R., Atreya, S. K., Franz, H., Wong, M., Conrad, P. G., et al. (2013). Abundance and isotopic composition of gases in the Martian atmosphere from the Curiosity rover. *Science*, *341*(6143), 263–266. https://doi.org/10.1126/science.1237966

Martinez, G. M., Newman, C., De Vicente-Retortillo, A., Fischer, E., Renno, N., Richardson, M., et al. (2017). The modern near-surface Martian climate: A review of in-situ meteorological data from Viking to Curiosity. *Space Science Reviews*, *212*(1–2), 295–338. https://doi.org/10.1007/s11214-017-0360-x

Martínez, G. M., Sebastián, E., Vicente-Retortillo, A., Smith, M., Johnson, J., Fischer, E., et al. (2023). Surface energy budget, albedo, and thermal inertia at Jezero Crater, Mars, as observed from the Mars 2020 MEDA instrument. *Journal of Geophysical Research: Planets*, *128*(2), e2022JE007537. https://doi.org/10.1029/2022je007537

Millour, E., Forget, F., Spiga, A., Vals, M., Zakharov, V., & Montabone, L. (2018). Mars climate database. In *From Mars express to ExoMars* (pp. 27–28).

Mimoun, D., Cadu, A., Murdoch, N., Chide, B., Sournac, A., Parot, Y., et al. (2023). The Mars microphone onboard SuperCam. *Space Science Reviews*, *219*(1), 5. https://doi.org/10.1007/s11214-022-00945-9



21699100, 2024, 7, Downloaded from https://agupubs.onlinelibrary.wiley.com/doi/10.1029/2024JE008469 by Cochrane France, Wiley Online Library on [12/12/2024]. See the Terms and Conditions (https://onlinelibrary.wiley.com/terms-and-conditions) on Wiley Online Library for rules of use; OA articles are governed by the applicable Creative Commons License

Munguira, A., Hueso, R., Sánchez Lavega, A. M., de la Torre Juárez, M., Martínez, G., Newman, C. E., et al. (2023). Near surface atmospheric temperatures at Jezero from Mars 2020 MEDA measurements. *Journal of Geophysical Research: Planets*, *128*(3), e2022JE007559. https://doi.org/10.1029/2022JE007559

Murdoch, N., Stott, A. E., Gillier, M., Hueso, R., Lemmon, M., Martinez, G., et al. (2022). The sound of a Martian dust devil. *Nature Communications*, *13*(1), 7505. https://doi.org/10.1038/s41467-022-35100-z

Newman, C. E., Hueso, R., Lemmon, M. T., Munguira, A., Vicente-Retortillo, A., Apestigue, V., et al. (2022). The dynamic atmospheric and aeolian environment of Jezero crater, Mars. *Science Advances*, *8*(21), eabn3783. https://doi.org/10.1126/sciadv.abn3783

Ostashev, V., & Wilson, D. (2000). Relative contributions from temperature and wind velocity fluctuations to the statistical moments of a sound field in a turbulent atmosphere. *Acta Acustica United with Acustica*, *86*(2), 260–268.

Ostashev, V. E. (2016). Acoustics in moving inhomogeneous media.

Petculescu, A., & Lueptow, R. M. (2007). Atmospheric acoustics of Titan, Mars, Venus, and Earth. *Icarus*, *186*(2), 413–419. https://doi.org/10.1016/j.icarus.2006.09.014

Petrosyan, A., Galperin, B., Larsen, S. E., Lewis, S. R., Määttänen, A., Read, P. L., et al. (2011). The Martian atmospheric boundary layer. *Reviews of Geophysics*, *49*(3), RG3005. https://doi.org/10.1029/2010RG000351

Polkko, J., Hieta, M., Harri, A., Tamppari, L., Martínez, G., Viúdez Moreiras, D., et al. (2023). Initial results of the relative humidity observations by MEDA instrument onboard the Mars 2020 Perseverance Rover. *Journal of Geophysical Research: Planets*, *128*(2), e2022JE007447. https://doi.org/10.1029/2022JE007447

Salomons, E. M. (2001). *Computational atmospheric acoustics*. Springer Netherlands. https://doi.org/10.1007/978-94-010-0660-6

Savijärvi, H., Martinez, G., Fischer, E., Rennó, N., Tamppari, L., Zent, A., & Harri, A.-M. (2020). Humidity observations and column simulations for a warm period at the Mars Phoenix lander site: Constraining the adsorptive properties of regolith. *Icarus*, *343*, 113688. https://doi.org/10.1016/j.icarus.2020.113688

Savijärvi, H., McConnochie, T. H., Harri, A.-M., & Paton, M. (2019). Water vapor mixing ratios and air temperatures for three Martian years from Curiosity. *Icarus*, *326*, 170–175. https://doi.org/10.1016/j.icarus.2019.03.020

Smith, M. D., Wolff, M. J., Spanovich, N., Ghosh, A., Banfield, D., Christensen, P. R., et al. (2006). One Martian year of atmospheric observations using MER Mini-TES. *Journal of Geophysical Research*, *111*(E12), E12S13. https://doi.org/10.1029/2006je002770

Smith, P. H. (2004). The phoenix mission to Mars. In *2004 IEEE aerospace conference proceedings (IEEE cat. no. 04TH8720)* (Vol. 1). IEEE. https://doi.org/10.1109/aero.2004.1367617

Stott, A. E., Murdoch, N., Gillier, M., Banfield, D., Bertrand, T., Chide, B., et al. (2023). Wind and turbulence observations with the Mars microphone on Perseverance. *Journal of Geophysical Research: Planets*, *128*(5), e2022JE007547. https://doi.org/10.1029/2022JE007547

Towner, M. C., Garry, J. R. C., Lorenz, R. D., Hagermann, A., Hathi, B., Svedhem, H., et al. (2006). Physical properties of Titan's surface at the Huygens landing site from the Surface Science Package Acoustic Properties sensor (API-S). *Icarus*, *185*(2), 457–465. https://doi.org/10.1016/j.icarus.2006.07.013

Vaughan, A., Minitti, M. E., Cardarelli, E. L., Johnson, J. R., Kah, L. C., Pilleri, P., et al. (2023). Regolith of the crater floor units, Jezero crater, Mars: Textures, composition, and implications for provenance. *Journal of Geophysical Research: Planets*, *128*(3), e2022JE007437. https://doi.org/10.1029/2022JE007437

Venegas, R., Boutin, C., & Umnova, O. (2017). Acoustics of multiscale sorptive porous materials. *Physics of Fluids*, *29*(8), 082006. https://doi.org/10.1063/1.4999053

Viúdez-Moreiras, D., de la Torre, M., Gómez-Elvira, J., Lorenz, R. D., Apéstigue, V., Guzewich, S., et al. (2022). Winds at the Mars 2020 landing site. 2. Wind variability and turbulence. *Journal of Geophysical Research: Planets*, *127*(12), e2022JE007523. https://doi.org/10.1029/2022JE007523

Viúdez-Moreiras, D., Lemmon, M., Newman, C. E., Guzewich, S., Mischna, M., Gómez-Elvira, J., et al. (2022). Winds at the Mars 2020 landing site: 1. Near-surface wind patterns at Jezero crater. *Journal of Geophysical Research: Planets*, *127*(12), e2022JE007522. https://doi.org/10.1029/2022JE007522

West, M., Gilbert, K., & Sack, R. (1992). A tutorial on the parabolic equation (PE) model used for long range sound propagation in the atmosphere. *Applied Acoustics*, *37*(1), 31–49. https://doi.org/10.1016/0003-682x(92)90009-h

Williams, J.-P. (2001). Acoustic environment of the Martian surface. *Journal of Geophysical Research*, *106*(E3), 5033–5041. https://doi.org/10.1029/1999JE001174

Wilson, D. K. (2000). A turbulence spectral model for sound propagation in the atmosphere that incorporates shear and buoyancy forcings. *Journal of the Acoustical Society of America*, *108*(5), 2021–2038. https://doi.org/10.1121/1.1311779

Zou, Y., Zhu, Y., Bai, Y., Wang, L., Jia, Y., Shen, W., et al. (2021). Scientific objectives and payloads of Tianwen-1, China's first Mars exploration mission. *Advances in Space Research*, *67*(2), 812–823. https://doi.org/10.1016/j.asr.2020.11.005



21699100, 2024, 7, Downloaded from https://agupubs.onlinelibrary.wiley.com/doi/10.1029/2024JE008469 by Cochrane France, Wiley Online Library on [12/12/2024]. See the Terms and Conditions (https://onlinelibrary.wiley.com/terms-and-conditions) on Wiley Online Library for rules of use; OA articles are governed by the applicable Creative Commons License